Specialisation of meiotic kinetochores revealed through a synthetic spindle assembly checkpoint strategy

Lori B Koch[1], Tiasha Ghosh[1], Christos Spanos[1,2], and Adele L Marston[1,2]*

* Correspondence to: adele.marston@ed.ac.uk

[1]Centre for Cell Biology, School of Biological Sciences, University of Edinburgh, Edinburgh EH9 3BF, UK.
[2]Discovery Research Platform for Hidden Cell Biology, School of Biological Sciences, University of Edinburgh, Edinburgh EH9 3BF, UK.

Abstract

Meiosis creates haploid gametes through two sequential M phases. While many studies have focused on meiosis I, the molecular events which drive and define meiosis II are largely unknown. Here, we report a novel cell synchronization strategy which allows for collection of yeast cells arrested at metaphase I or metaphase II, enabling better characterisation of meiosis II events. The method relies on chemically-inducible dimerization of ectopic copies of spindle assembly checkpoint (SAC) proteins Mps1 and Spc105. Using this synthetic SAC (SynSAC) approach, we found that the SAC response is weaker in metaphase I compared to metaphase II and that the PP1 binding site within Spc105 contributes to restraining the MI SAC response. Furthermore, we demonstrate the utility of the SynSAC approach by analysing the composition and phosphorylation of kinetochores from metaphase I and metaphase II. This revealed an increase in the abundance of outer kinetochore proteins in meiotic metaphase I and reduced phosphorylation on metaphase II kinetochore proteins. Overall, we present the SynSAC method as a valuable tool for analysis of both meiotic metaphases.

Introduction

To make haploid gametes for sexual reproduction, diploid cells undergo meiosis which consists of a single round of DNA replication followed by two sequential chromosome segregation events, meiosis I and meiosis II. In meiosis I, maternal and paternal chromosomes, called homologs, separate, while in meiosis II, sister chromatids separate, similar to mitosis. To achieve this, the sister chromatids within each homolog are mono-oriented toward the same spindle pole in meiosis I but bi-oriented towards opposite poles in meiosis II. This requires that kinetochores, large protein complexes which connect chromosomes to spindle microtubules, establish mono-orientation in meiosis I and then convert to bi-orientation in meiosis II. The sequential segregation of homologs and sister chromatids further rely on the step-wise loss of sister chromatid cohesion coupled to two consecutive rounds of spindle assembly and disassembly (reviewed in (Duro and Marston, 2015)). How these key cell biological events are established and coupled in meiosis to allow two distinct rounds of chromosome segregation without an intervening S phase is not well understood. In human oocytes, meiotic chromosome segregation is error-prone and aneuploidy is common (Gruhn and Hoffmann, 2022). Thus identifying molecular mechanisms which prevent improper chromosome segregation may help efforts to improve fertility.

A major barrier in defining molecular events that direct the two meiotic divisions is a lack of synchronization tools which allow collection of populations of cells at key meiotic stages. While mammalian oocytes naturally arrest in metaphase II, material is limited, which precludes biochemical analysis. *Xenopus* oocytes provide a powerful system for analysis of metaphase II extracts but isolation of pure metaphase I populations is challenging (Iwabuchi et al., 2000; Peshkin et al., 2025). Furthermore, identifying chromosome-related proteins in the comparatively large cytoplasmic volume of oocytes presents an additional impediment.

The ability to harvest large number of cells together with ease of genetic manipulation have made yeast outstanding tools for discovering the fundamental mechanisms of meiosis. However, compared to mitosis, our knowledge of meiotic chromosome segregation has lagged behind, in part due to a lack of robust synchronization systems. Nevertheless, recent advances allow reversible arrest of budding yeast at meiotic entry and prophase, allowing synchronous release into meiosis I, and subsequently meiosis II (Berchowitz et al., 2013; Carlile and Amon, 2008; Chia and van Werven, 2016). These systems have been used extensively, but the short time window between the divisions limits the ability to resolve pure meiosis I and II populations. Therefore, direct comparison of meiosis I and II has remained difficult to achieve in any system.

102 To overcome these challenges, we sought to establish a method that relies on
103 inducible inhibition of the Anaphase Promoting Complex (APC-Cdc20) in either meiosis I or
104 meiosis II. The APC-Cdc20 is a ubiquitin ligase that targets key substrates for degradation
105 including securin and cyclin B, which is required for progression into anaphase (Peters, 2006).
106 The requirement for the APC-Cdc20 at both meiosis I and II is well-established and placement
107 of the gene for the APC activator, *CDC20*, under control of a meiotically-repressed promoter
108 has been widely used to arrest budding yeast cells in metaphase I (Lee and Amon, 2003).
109 This system has also been adapted to allow re-expression of *CDC20* and synchronous
110 meiosis II entry (Argüello-Miranda et al., 2017) as well as re-expression of the *cdc20-3*
111 temperature sensitive allele to enable collection of metaphase II cells (Mengoli et al., 2021).
112 However, the reliance on transcriptional control and temperature shift results in a slower
113 response than desirable. Therefore, no tools currently exist to quickly and reliably enrich
114 budding yeast cell populations in meiosis II.
115 The APC-Cdc20 is a natural target of the spindle assembly checkpoint (SAC), a
116 signalling cascade that prevents anaphase when chromosomes are not properly attached to
117 the spindle (McAinsh and Kops, 2023). The SAC is initiated at improperly attached
118 kinetochores when the kinase Mps1 phosphorylates the kinetochore protein Spc105^{KNL1}. This
119 phosphorylation recruits the checkpoint proteins Bub3/Bub1 and then Mad1/Mad2 to the
120 kinetochore. Within this kinetochore complex, Mad2 is converted from the open to closed
121 conformation and C-Mad2 associates with Mad3^{BubRI}, Bub3, and Cdc20 to form the mitotic
122 checkpoint complex (MCC), a diffusible inhibitor of the anaphase promoting complex (APC).
123 Sustained SAC activation, resulting in prometaphase arrest, can be induced experimentally
124 by perturbing kinetochore-microtubule interactions, for example by treatment with
125 microtubule-depolymerizing drugs, and this method has been used extensively in mitotic cells.
126 However, meiotic cells respond poorly to such drugs, likely due to a combination of impaired
127 uptake, toxicity and a weakened checkpoint (Hochwagen et al., 2005; MacKenzie et al., 2023).
128 Moreover, such treatments are unsuitable for analysis of kinetochore function since they
129 ablate microtubule interactions and convert kinetochores into a signalling platform, thereby
130 changing their composition and properties.
131 An alternative approach to arrest cells in either metaphase I or II would induce SAC-
132 dependent APC-Cdc20 inhibition without perturbing kinetochores. Mechanistic studies in
133 fission yeast and human cells have achieved inducible activation of the SAC through
134 conditional dimerization of Mps1 kinase and Spc105^{KNL1} (Amin et al., 2018; Aravamudhan et
135 al., 2015; Chen et al., 2019; Leontiou et al., 2019). Here, we adapted this approach to arrest
136 cells in either metaphase I or metaphase II of meiosis. We demonstrate that induced

137 dimerization of Mps1 and Spc105^{KNL1} engineered to lack their kinetochore-targeting domains
138 efficiently arrests cells in either metaphase I or metaphase II, in addition to mitotic metaphase.
139 This synthetic SAC (SynSAC)-dependent arrest relies on the same downstream signalling
140 cascade required for APC-Cdc20 inhibition during mitotic division, culminating in stabilization
141 of the anaphase inhibitor Pds1^{securin}. We find that the SynSAC arrest is more potent in
142 metaphase II than metaphase I, and provide evidence that protein phosphatase 1 (PP1) limits
143 the duration of the SAC-mediated metaphase I delay. To demonstrate the utility of our SynSAC
144 approach, we purified kinetochores from metaphase I, metaphase II, and mitotic metaphase
145 SynSAC cells and analysed their composition and phosphorylation using mass spectrometry.
146 This provided evidence that the relative enrichment of purified core kinetochore sub-
147 complexes changes in meiotic metaphase I and II compared to mitotic metaphase, and that
148 overall kinetochore phosphorylation is reduced in metaphase II. Therefore, by developing
149 SynSAC as a meiotic interrogation tool we have generated a comprehensive dataset of
150 kinetochore composition and phosphorylation, a key resource to uncover the critical
151 specializations that direct distinct segregation events in meiosis I and II.
152
153 **Results**
154 ***A synthetic SAC prolongs metaphase I or metaphase II***
155 We sought to activate the SAC to arrest cells in metaphase without disrupting kinetochores.
156 Thus, we constructed a yeast strain which has an additional, ectopic copy of each of Spc105
157 and Mps1 lacking their kinetochore-binding domains and which can be inducibly dimerised.
158 To temporally separate populations of cells undergoing meiosis I vs meiosis II, this strain also
159 carried inducible *NDT80*, which allows synchronous release from prophase arrest upon
160 addition of β-estradiol (Carlile and Amon, 2008). To induce dimerization, we used the PYL and
161 ABI tags, which dimerise in the presence of the plant hormone abscisic acid (ABA) (Liang et
162 al., 2011; Miyazono et al., 2009). This system is particularly advantageous compared with the
163 widely used rapamycin-inducible dimerization system because it cannot affect endogenous
164 mTOR signalling, nor does it require background mutations to avoid toxicity. Spc105 lacking
165 its C-terminal kinetochore localization domain (Ghodgaonkar-Steger et al., 2020; Maskell et
166 al., 2010; Petrovic et al., 2014; Roy et al., 2022), and tagged with PYL, was produced from its
167 endogenous promoter (Spc105$^{(1-455)}$-PYL). Similarly, the C-terminal kinase domain of Mps1,
168 also under the control of its native promoter and lacking the N-terminal disordered domain
169 which mediates its kinetochore localization, was fused to ABI (Mps1$^{(440-765)}$-ABI) (Figure
170 1A)(Araki et al., 2010). As expected, spore viability of this “SynSAC” strain after prophase

171 release was comparable to that of a strain lacking the ABI/PYL tagged truncations, indicating
172 that meiosis was not impaired by these constructs (Figure 1B).
173 We scored spindle morphology after anti-tubulin immunofluorescence to determine cell
174 cycle stage (Figure 1C). Prophase, metaphase I, anaphase I, metaphase II, anaphase II and
175 post-meiotic spindles appeared successively over the timecourse in both the absence and
176 presence of ABA (Figure 1D). While SynSAC dimerisation did not alter characteristic spindle
177 morphologies, it changed their distribution over time. Following prophase release in the
178 absence of ABA, metaphase I and metaphase II cell populations peak at approximately 75
179 and 120 min, respectively, as determined by spindle morphology (Figure 1E). ABA addition at
180 prophase release extended metaphase I by 15 minutes and metaphase II by 30 minutes
181 (Figure 1E). This suggested that conditional dimerization of Spc105$^{(1-455)}$-PYL and Mps1$^{(440-}$
182 $^{765)}$-ABI is sufficient to activate the SAC and delay cells in either metaphase I or metaphase II.
183 To delay cells specifically at metaphase II, we added ABA at 100 minutes after prophase
184 release, corresponding to the anaphase I peak according to spindle morphology, and this
185 resulted in a pronounced (60 min) metaphase II delay (Figure 1E).
186 To confirm that the delay in cell cycle progression was dependent on the canonical
187 spindle checkpoint cascade, we tested whether the SynSAC-induced metaphase delays
188 required downstream SAC proteins. Deletion of *MAD2* or *MAD3* abolished the SynSAC delays
189 in metaphase I and II, since cell cycle profiles were comparable when either ethanol or ABA
190 were added at prophase release (Figure 2A and B). Similarly, SynSAC dimerization after
191 meiosis I did not delay cells in metaphase II in the absence of the SAC proteins (Figure 2C).
192 Therefore, both meiotic metaphase delays induced by dimerization of Mps1$^{(440-765)}$-ABI and
193 Spc105$^{(1-455)}$-PYL are dependent on known downstream SAC components. We conclude that
194 SynSAC can induce a delay in both metaphase I and metaphase II, in a manner requiring
195 downstream checkpoint components.
196
197 **Metaphase I, metaphase II and mitotic metaphase show differential sensitivity to**
198 **SynSAC**
199 We noticed that SynSAC induced a more pronounced delay in metaphase II than metaphase
200 I (Figure 1E, Figure 2B and C). Furthermore, both the metaphase I and metaphase II arrests
201 were transient and cells subsequently underwent both meiotic divisions to produce spores,
202 even in the presence of ABA. In contrast, SynSAC induced a robust mitotic metaphase arrest
203 and checkpoint-dependent growth inhibition (Figure 2-figure supplement 1A and B). This is in
204 accordance with findings in yeast and vertebrates which have suggested that the SAC is less
205 robust in meiosis I compared to either mitotic metaphase or metaphase II (Gui and Homer,

206 2012; Kolano et al., 2012; Lane et al., 2012; MacKenzie et al., 2023; Nagaoka et al., 2011;
207 Sebestova et al., 2012). However, since these previous observations rely on methods which
208 perturb kinetochore-microtubule attachments, it has remained unclear whether this difference
209 stems from reduced SAC signalling or a dampened response. Our finding that SynSAC, which
210 uncouples signal generation from the response, induces a graded effect, demonstrates that
211 meiosis I and to a lesser extent meiosis II have a reduced response to checkpoint signalling.
212 To explore the differences between the meiosis I and II SAC responses further, we
213 analysed the effects of SynSAC on downstream signalling events. The SAC inhibits the APC-
214 Cdc20 from targeting the anaphase inhibitor securin for degradation. Therefore, we monitored
215 Pds1^{securin} degradation as a readout for APC-Cdc20 activity in the SynSAC strain. Without
216 ABA-induced dimerization, Pds1^{securin} levels decreased along with the appearance of
217 anaphase I spindles at 90 minutes after prophase release, re-accumulated at 105 minutes,
218 then decreased again at 135 minutes when anaphase II spindles appeared (Figure 3A). In
219 wild-type cells, Pds1 levels are higher in meiosis I than in meiosis II, likely because the interval
220 between the divisions is too short to allow Pds1 reaccumulation (Marston et al., 2003; Matos
221 et al., 2008; Salah and Nasmyth, 2000). This pattern was also observed in SynSAC strains in
222 the absence of ABA (Figure 3A). Note that Pds1 levels do not fully decline in this population-
223 based analysis as the short duration of meiotic stages results in a mixed-stage population. For
224 example, at the anaphase I peak (90 minutes) around 30% of cells remain in prior stages in
225 which Pds1 levels are expected to be high. However, ABA addition at the time of prophase
226 release resulted in Pds1^{securin} stabilisation throughout the time course, consistent with delays
227 in both metaphase I and metaphase II (Figure 3B). Anaphase I spindles nevertheless
228 appeared with delayed kinetics, peaking at ~40% at 105 min. Concurrently, ~40% of cells
229 remained in metaphase I or II and were therefore Pds1-positive, accounting for the persistent
230 Pds1 signal on the western blot. In contrast, anaphase II spindles are observed at low
231 frequency (maximum 10%) from 165 minutes onwards because metaphase II spindles give
232 way to post-meiotic spindles, without undergoing anaphase II extension (Figure 1D).
233 Therefore, SynSAC activation prior to metaphase I stabilises Pds1^{securin} with the greatest effect
234 in meiosis II. When ABA was added after metaphase I at 100 minutes after release, Pds1^{securin}
235 levels similarly remained high until the end of the timecourse and after spindle disassembly
236 (Figure 3C). Together, these findings suggest that activation of the SynSAC in meiosis delays
237 metaphase I and II by preventing Pds1^{securin} degradation. Interestingly, although SynSAC
238 induces a longer delay in metaphase II compared to metaphase I, in both cases the delay is
239 transient and accompanied by Pds1^{securin} persistence.

240 One possibility for the extended delay in metaphase I compared to metaphase II could
241 be differential protein expression in the two divisions. To test this, we assessed the levels of
242 the SynSAC dimerising proteins by Western blotting. Both full length endogenous and the C-
243 terminal SynSAC fragment of Mps1 were tagged with 3V5 for direct comparison, which
244 revealed increased expression of Mps1$^{(440-765)}$-ABI-3V5 compared to Mps1-V5 (Figure 3-figure
245 supplement 1A and B), consistent with the presence of a degron in the N-terminal domain of
246 Mps1 (Palframan et al., 2006). However, levels of the SynSAC Mps1$^{(440-765)}$-ABI-3V5 fragment
247 were relatively consistent throughout meiosis I and II (Figure 3-figure supplement 1A and B).
248 Similarly, FLAG-tagging of both full length endogenous Spc105 and Spc105$^{(1-455)}$-PYL
249 indicated that protein levels were equivalent across the two divisions (Figure 3-figure
250 supplement 1C and D). Thus, temporal differences in the abundance of the SynSAC
251 dimerising constructs cannot account for the longer delay in metaphase II compared to
252 metaphase I.
253 Finally, the transience of the SynSAC delay at both metaphase I and metaphase II
254 raised the question of whether escape into anaphase I and II was associated with accurate
255 chromosome segregation. To test this, SynSAC strains were allowed to complete sporulation
256 in the presence of ABA and spore viability was measured. If kinetochores or chromosome
257 segregation were significantly disrupted by the delayed meiotic cell cycle, spores would inherit
258 the incorrect number of chromosomes and be inviable. However, spore viability after SynSAC
259 dimerization, either before metaphase I or specifically in metaphase II, was not significantly
260 different from wild type (Figure 3-figure supplement 2). Therefore, SynSAC does not disrupt
261 chromosome segregation and provides a powerful tool to study meiotic metaphase.
262
263 ***PP1 binding to Spc105 limits SAC-induced metaphase delay in meiosis***
264 Why does SynSAC induce a more potent arrest in metaphase II compared to metaphase I?
265 One possibility is that checkpoint silencing mechanisms are especially active in meiosis I and
266 could contribute to a rapid reversal of the checkpoint activity. A key event in checkpoint
267 silencing is the docking of Protein Phosphatase 1 (PP1; Glc7 in yeast) onto two consensus
268 motifs in the N-terminal region of Spc105, leading to the dephosphorylation of Spc105 and the
269 disassembly of the SAC signalling platform (Rosenberg et al., 2011; Roy et al., 2019). Analysis
270 of mitotic cells indicated that the RVxF motif is the primary PP1 docking motif and that the
271 SILK motif (GILK in budding yeast) plays an auxiliary role (Rosenberg et al., 2011; Roy et al.,
272 2019). To test whether PP1 binding to Spc105 regulates the duration of the SynSAC delay in
273 meiosis, we created strains in which the dimerizing copy of Spc105$^{(1-455)}$-PYL in the SynSAC
274 strain background had mutations in the RVxF and SILK motifs that would prevent PP1 binding.

275 We mutated either the SILK motif, creating *spc105*$^{(1-455)}$*-4A-PYL*, or the RVSF motif, creating
276 *spc105*$^{(1-455)}$*-RASA-PYL*, and additionally generated *spc105*$^{(1-455)}$*-4A-RASA* which has both
277 PP1-binding motifs mutated. We also made the *spc105*$^{(1-455)}$*-RVAF* mutant in which serine 77
278 within the RVSF motif is mutated to alanine, to block potential Ipl1$^{\text{Aurora B}}$ phosphorylation of
279 this site. In human cells, Aurora B-dependent phosphorylation of KNL1$^{\text{Spc105}}$ within the RVSF
280 motif appears to prevent PP1 binding (Liu et al., 2010). However, the phospho-null RVAF
281 mutant does not impact growth of budding yeast, suggesting it may not have as much
282 importance in this organism (Rosenberg et al., 2011; Roy et al., 2019).
283 In the absence of ABA, mutation of the PP1 binding sites in the SynSAC construct did
284 not affect meiotic progression or spore viability (Figure 4-figure supplement 1A and B), nor did
285 they compromise mitotic growth (Figure 4-figure supplement 1C). However, activating the
286 SynSAC by adding ABA at the time of prophase release resulted in a metaphase I delay of
287 varying duration depending on the status of the PP1-binding motifs (Figure 4A). Mutation of
288 the SILK motif (*spc105*$^{(1-455)}$*-4A*) did not detectably alter the 15-30 min metaphase I delay
289 observed for the wild-type SynSAC (Figure 4A), consistent with the notion that this motif is
290 less important. However, preventing PP1 binding to the RVxF motif (*spc105*$^{(1-455)}$*-RASA*)
291 extended the duration of the SynSAC-induced metaphase I delay considerably and mutation
292 of both PP1 binding motifs (*spc105*$^{(1-455)}$*-4A-RASA*) led to an even more pronounced delay,
293 with metaphase I cells persisting until the end of the timecourse (Figure 4A). Conversely,
294 mutation of the potential Ipl1$^{\text{Aurora B}}$-dependent kinase site (*spc105*$^{(1-455)}$*-RVAF*), which is
295 predicted to increase PP1 binding and thereby promote checkpoint silencing, modestly
296 decreased the duration of the metaphase I delay (Figure 4A). Taken together, these findings
297 indicate that PP1 binding to Spc105 dampens the SynSAC response in meiosis I and that both
298 PP1 binding motifs play a role, with the RVxF motif being the primary binding site.
299 To test whether the duration of the metaphase II delay is also affected by the ability of
300 PP1 to bind Spc105, we repeated the above experiment except ABA was added only at the
301 time of anaphase I. As for metaphase I, preventing PP1 binding to Spc105 increased the
302 duration of SynSAC-induced metaphase II, with the different mutations showing a gradient of
303 effects (Figure 4B). The strongest metaphase II delay was observed with the *spc105*$^{(1-455)}$*-4A-*
304 *RASA* construct, with the *spc105*$^{(1-455)}$*-RASA* mutant alone also extending metaphase II
305 compared to the wild-type, as judged by the absence of anaphase II cells. Mutation of the
306 SILK motif (*spc105*$^{(1-455)}$*-4A*) caused a modest additional 15 minutes delay. However, we
307 observed no detectable effect of mutating the potential Ipl1$^{\text{Aurora B}}$ site on the SynSAC
308 metaphase II delay (Figure 4B). Overall, these results indicate that PP1 binding to the RVxF
309 motif, and to a lesser extent the SILK motif, on Spc105 affects the duration of the metaphase

310 to anaphase transition in both meiosis I and II. Interestingly, the effect on metaphase I appears
311 more striking, potentially suggesting increased PP1-dependent SAC silencing activity in
312 meiosis I. These findings also indicate that *spc105*$^{(1-455)}$*-4A-RASA* is the preferred SynSAC
313 variant, particularly where metaphase I arrest is the goal. However, due to concurrent
314 investigations, below we employed the simple SynSAC system and demonstrate its suitability
315 for functional studies.
316
317 ***Kinetochore composition changes at meiotic prophase, metaphase I, and metaphase II***
318 The SynSAC system we developed allows robust isolation of populations of both metaphase
319 I and metaphase II cells from the same strain, providing the first opportunity for biochemical
320 comparisons between these stages. As proof-of-principle, we analysed kinetochores, which
321 must be modified to achieve distinct functions during meiosis. Indeed, previous work has
322 established a dramatic remodelling of kinetochore composition between meiotic prophase and
323 meiosis I (Borek et al., 2021; Meyer et al., 2015). However, the lack of a suitable arrest system
324 precluded analysis of meiosis II. Since kinetochores undergo a configuration switch from
325 mono-oriented in meiosis I to bi-oriented in meiosis II to direct the successive segregation of
326 homologs and sister chromatids, direct comparison of meiosis I and meiosis II kinetochores is
327 an important goal. We exploited our newly developed SynSAC system to determine
328 kinetochore composition at metaphase I and metaphase II, together with mitotic metaphase
329 and meiotic prophase for comparison. To do so, we purified kinetochores via
330 immunoprecipitation of the central kinetochore protein Dsn1 and used mass spectrometry to
331 analyse their composition (Akiyoshi et al., 2010; Borek et al., 2021; Sarangapani et al., 2014).
332 Metaphase arrests were confirmed by spindle immunofluorescence (Figure 5-figure
333 supplement 1A) and silver staining indicated broadly similar purifications across replicates and
334 cell cycle stages (Figure5-figure supplement 1B).
335 To determine kinetochore composition, we used data independent acquisition (DIA)
336 mass spectrometry. Due to the high sensitivity of this method, thousands of proteins were
337 quantified in each of three replicate immunoprecipitations from each stage (Figure 5-figure
338 supplement 2A) and 2,415 quantified proteins were common to all three replicates of the Dsn1-
339 His-FLAG IPs from all 4 cell cycle stages (Figure 5-figure supplement 2B). Consistent trends
340 in kinetochore protein abundance were observed across replicates (Figure 5-figure
341 supplement 2C). As expected, Dsn1 and other components of the core kinetochore structure,
342 especially other members of the KMN (KNL1^{Spc105}-Mis12^{MIND}-Ndc80) network were most
343 enriched compared to the untagged control immunoprecipitations (Figure 5A-E). Spindle pole
344 body and microtubule-associated proteins were enriched in mitotic metaphase, meiotic

345 metaphase I and metaphase II, but depleted from prophase kinetochore purification, along
346 with outer kinetochore (Mis12^{MIND}-Ndc80) complexes (Figure 5B-E) (Borek et al., 2021; Meyer
347 et al., 2015).

348 To better quantify differences in kinetochore protein abundances between the different
349 cell cycle stages, we scaled all protein abundances to the level of Dsn1 quantified in each
350 individual sample (Figure 6-figure supplement 1). As expected, the abundance of most
351 kinetochore proteins was slightly lower than the bait protein Dsn1 in *DSN1-His-Flag* ("tag")
352 samples, but not in the *DSN1* negative control immunoprecipitations ("no tag") (Figure 6-figure
353 supplement 1D). Overall, there was an increased amount of quantified protein in the prophase
354 and metaphase I kinetochore ("tag") samples compared to the metaphase II and mitotic
355 metaphase samples (Figure 6-figure supplement 1E). Although this difference was not
356 significant when the levels of known kinetochore proteins were compared (Figure 6-figure
357 supplement 1F), it is possible that it reflects increased stability and/or dynamics of protein-
358 protein interactions with the kinetochore in prophase and metaphase I.

359 Next, we performed pair-wise comparisons to identify which proteins, relative to Dsn1,
360 were the most different in abundance between cell cycle stages (Figure 6). In addition, we
361 used GO term analysis to identify shared functions among the top 50 non-kinetochore proteins
362 associated with the Dsn1 immunoprecipitate at each stage (Figure 6-figure supplement 2A).
363 At prophase, proteins involved in chromosome pairing, recombination, and respiration were
364 associated with kinetochores (Figure 6-figure supplement 2A and B). At metaphase I,
365 chromosome organization, spindle pole body, and spindle organization proteins were
366 enriched. The enrichment of many chromatin-associated factors, e.g. histones and chromatin
367 remodeling complexes, with metaphase I, but not metaphase II kinetochores (Figure 6-figure
368 supplement 2A and B) is consistent with closer association of kinetochores with chromatin in
369 the mono-oriented vs bi-oriented state. At metaphase II, sporulation and spore wall proteins
370 became enriched (Figure 6-figure supplement 2A and B). Mitotic kinetochores were
371 associated with nucleolar, ribosome, and nuclear envelope proteins (Figure 6-figure
372 supplement 2A and B). Together, these associations underscore the dynamic nature of
373 kinetochore protein interactions. Further, it suggests that the kinetochore may serve as a
374 platform to direct cell cycle stage-specific signalling such as promoting recombination at
375 meiotic prophase, specialised kinetochore-spindle associations at metaphase I and instigating
376 meiotic-exit processes such as spore wall formation in metaphase II.

377 Beyond identifying novel protein interactions, we aimed to determine whether there
378 were significant changes in the kinetochore composition itself at the different stages, relative
379 to Dsn1. Across the 4 stages, we were able to quantify ~70 known kinetochore proteins (Figure

380 7A). As expected, proteins within the KMN network, which Dsn1 is a part of, were most
381 abundant, while proteins at the inner or outer edges of the complex, or only transiently
382 associated, were less abundant. Comparing protein abundances grouped by sub-complex or
383 function at each stage indicated that inner kinetochore CCAN proteins were reduced at meiotic
384 metaphase I and II compared to prophase or mitotic metaphase, although the trend was not
385 significant, while outer kinetochore Dam1 complex proteins showed the reverse trend (Figure
386 7A-B). It is possible that meiotic kinetochores are enriched in outer kinetochore complexes to
387 facilitate the challenge of capturing homologs in meiosis I. Alternatively, inner kinetochore
388 protein interactions may be weakened in the two meiotic metaphases, while outer kinetochore
389 interactions are better preserved during the purification. As expected, there was a significant
390 depletion of the Ndc80 and Dam1 complex proteins from kinetochores in prophase, in
391 agreement with previous observations (Chen et al., 2020; Hayashi et al., 2006; Meyer et al.,
392 2015; Miller et al., 2012) (Figure 7A-B).
393 Within the diverse kinetochore "accessory" group, the strongest changes were an
394 enrichment of Glc7^{PP1} phosphatase regulator Fin1 at meiotic metaphase I and II, as well as
395 an enrichment in Glc7^{PP1} phosphatase at prophase. Additionally, proteins with known
396 functions in mono-orientation such as monopolin complex proteins Csm1 and Mam1 had
397 higher abundance or were exclusively detected in metaphase I but not metaphase II
398 kinetochores. SAC and CPC protein abundance on kinetochores was largely comparable in
399 all stages, other than a depletion in Mps1 levels at prophase, which likely reflects the fact that
400 this is the only condition in which SynSAC was not induced. Finally, microtubule-associated
401 proteins (MAPs) were relatively depleted from mitotic kinetochores and the Bik1$^{CLIP-170}$
402 microtubule plus-end tracking protein was particularly enriched on metaphase I and
403 metaphase II kinetochores, consistent with the general increase in abundance of the
404 microtubule-binding components of the outer kinetochore in these purifications (Figure 7A-B).
405 Together, our results reveal that although the levels of most core kinetochore proteins are
406 relatively stable at different cell cycle stages, there are significant differences. Notably, there
407 is a loss of outer kinetochore proteins at prophase, a depletion in some inner kinetochore
408 protein interactions at meiotic metaphase vs mitotic, and an increase in outer kinetochore
409 protein levels at metaphase I, and also to some extent at metaphase II.
410
411 ***Reduced phosphorylation of kinetochores at metaphase II***
412 Protein composition changes are only partially responsible for the distinct behaviour of
413 kinetochores in meiosis I and meiosis II. Indeed, multiple kinases are known to contribute
414 (Clyne et al., 2003; Lee and Amon, 2003; Lo et al., 2008; Matos et al., 2008; Petronczki et al.,

415 2006), indicating that phosphorylation is a key mechanism driving these changes. However,
416 a global picture of phosphorylation changes at the kinetochore is lacking. This is challenging
417 because phospho-peptides are relatively low in abundance and recovery of sufficient
418 quantities of protein from highly synchronised cells is especially important to detect changes
419 between stages. Our SynSAC approach makes this possible because large quantities of
420 highly synchronised cells can be collected within a single experiment.

421 To this end, 95% of the eluates from the kinetochore purifications above were
422 subjected to phospho-peptide enrichment and DIA-MS. Thus, alongside quantification of the
423 kinetochore-associated proteome as described above, we obtained matched phospho-
424 proteomic datasets for each sample. Overall, we identified 4,480 phosphorylation sites
425 ("phospho-sites") on 1,614 proteins with 99% confidence. The abundance of each phospho-
426 site was normalised to the total abundance of the corresponding protein quantified in the non-
427 phospho-enriched fraction of the sample. This more accurately identifies dynamic
428 phosphorylation, rather than protein abundance. Additionally, we filtered the dataset to
429 analyse only those phospho-sites which were identified in all replicates of at least one sample
430 type. With these metrics, we quantified ~1,500 phosphorylation sites on meiotic prophase and
431 meiotic metaphase I kinetochores and ~700-1,100 phospho-sites on meiotic metaphase II and
432 mitotic metaphase kinetochores (Figure 8-figure supplement 1A). As expected, many
433 phosphorylation sites were stage-specific, with 177 sites identified in all replicates of all stages
434 (Figure 8-figure supplement 1B).

435 We performed GO term enrichment analysis to look for shared functions among the
436 phospho-proteins most abundant in the kinetochore purifications. This was done with the top
437 50 most abundant phospho-proteins which are not known kinetochore proteins, in order to
438 identify alternative processes. At prophase, phospho-proteins involved in chromosome
439 organization, double-strand break repair, and transcription were associated with kinetochores
440 (Figure 8-figure supplement 1C). Similarly, metaphase I phospho-proteins were involved in
441 chromatin remodeling, chromosome organization, and gene expression. At metaphase II,
442 phospho-proteins involved in cell cycle regulation, sexual reproduction, and spindle pole body
443 organization were enriched (Figure 8-figure supplement 1C). Finally, mitotic metaphase
444 phospho-proteins were involved in the microtubule cytoskeleton, nucleus organization, and
445 regulation of transcription. Overall, the temporal trends seen in the GO term analysis are
446 apparent in ranked lists of the most abundant non-kinetochore phospho-sites for each stage
447 comparison (Figure 8-figure supplement 1D).

448 To determine whether there were general trends in the total level of phosphorylation,
449 we analysed the distribution of kinetochore phospho-site abundances at the 4 different stages

450 (Figure 8). The number of phospho-sites on known kinetochore proteins was around ~100 at
451 each stage however the median level of phosphorylation was higher in meiotic prophase and
452 metaphase I than it was in metaphase II and mitotic metaphase (Figure 8A). This suggests
453 that kinetochores are subject to essential phosphorylation in meiosis I and that either
454 phosphatase activity increases, or kinase activity towards kinetochores decreases at
455 metaphase II. Interestingly, the total abundance of phosphorylation on kinetochores was very
456 similar between metaphase II and mitotic metaphase, suggesting that the increased level of
457 kinetochore phosphorylation is characteristic of meiosis I.

458 We next asked whether these phosphorylation events were focused on specific
459 kinetochore sub-complexes or functional groups. The CCAN and KMN subcomplexes
460 contained the most phosphorylation sites, while relatively few sites were mapped to the Cbf3
461 complex and MAPs (Figure 8A). The levels of phosphorylation on the CCAN and KMN
462 subcomplexes were highest in prophase and metaphase I, and lower in metaphase II and
463 mitotic metaphase, mirroring the trend seen for all kinetochore sites. Interestingly, there
464 appeared to be increased phosphorylation on outer kinetochore Dam1 complex proteins in
465 metaphase I vs II, and overall higher phosphorylation in meiosis vs mitosis. Since Dam1
466 complex proteins are known targets of error correction kinases Ipl1$^{\text{Aurora B}}$ and Mps1, this may
467 suggest increased error correction in meiosis vs mitosis. To identify which kinetochore
468 proteins were most phosphorylated, we calculated the sum of the abundance of all
469 phosphorylation sites on individual kinetochore proteins at each stage, and then ranked the
470 proteins based on the total sum from all stages (Figure 5B). This revealed that Spc105, Bir1,
471 Lrs4, Sli15, Dsn1, Okp1 and Ame1 were the most heavily phosphorylated kinetochore
472 proteins. Additionally, we determined the maximum range in abundance between cell cycle
473 stages for each phospho-site within each protein. This revealed that Mif2$^{\text{CENP-C}}$, Dsn1, Cin8$^{\text{Kif11}}$,
474 Okp1$^{\text{CENP-Q}}$, and Cse4$^{\text{CENP-A}}$ have highly dynamic phosphorylation sites (Figure 8C).

475 Finally, we highlight several individual phospho-sites with interesting trends (Figure
476 8D). Slk19$^{\text{CENP-F}}$ regulates both spindle stability and mitotic/meiotic exit (Buonomo et al., 2003;
477 Marston et al., 2003; Stegmeier et al., 2002; Sullivan et al., 2001). We found that
478 phosphorylation of Slk19-S-23, in part of the protein involved in meiotic exit (Havens et al.,
479 2010), is reduced in metaphase II. In mitosis, phosphorylation of the N-terminus of Ndc80 by
480 Ipl1$^{\text{Aurora B}}$ promotes detachment of kinetochores from microtubules, allowing for correction of
481 erroneous attachments (Akiyoshi et al., 2009; Pinsky et al., 2006; Sarangapani et al., 2013);
482 in meiosis, Ipl1$^{\text{Aurora B}}$ phosphorylation of an overlapping set of sites, including T54, destabilizes
483 Ndc80 protein levels in prophase, contributing to the loss of outer kinetochore proteins at this
484 time (Chen et al., 2020). Consistent with this, we observed significantly more phosphorylation

485 of Ndc80-T-54 on purified kinetochores in meiotic prophase and metaphase I (Figure 8D).
486 Dsn1-S-69 is found very close to where the monopolin complex that directs mono-orientation
487 in meiosis I is thought to bind (residues 72-110) (Plowman et al., 2019; Sarkar et al., 2013).
488 We observed greatest phosphorylation of Dsn1-S-69 in prophase and metaphase I, the time
489 when kinetochores prepare for mono-orientation, suggesting it may be a functionally important
490 modification (Figure 8D). Finally, we found that S70 phosphorylation on inner kinetochore
491 protein Okp1^{CENP-Q}, a likely Cdk substrate (Holt et al., 2009), is reduced at metaphase II.
492 To uncover trends in types of kinase activity directed towards kinetochore proteins,
493 we conducted motif analysis on phospho-sites at different cell cycle stages. Of the nearly 100
494 kinetochore phosphorylation sites identified, the most prominent trend was for a proline
495 residue at the +1 position from the phospho-acceptor site, which is a known motif recognised
496 by cyclin-dependent kinase (Cdk) as well as MAP kinases (Figure 9A). Next, we analysed how
497 many of the kinetochore phospho-sites at each stage matched a panel of known kinase
498 consensus motifs. The trends were weak suggesting common types of kinase activity at the
499 different stages, however, there was a slight preference for the strict Cdk or Ipl1$^{Aurora\ B}$ kinase
500 consensus motif among prophase phospho-sites compared with the other stages (Figure 9B).
501 Additionally, fewer sites matching the Ipl1$^{Aurora\ B}$ motif were found in meiotic metaphase I and
502 II (Figure 9B), which may suggest that Ipl1$^{Aurora\ B}$ activity is reduced at these times. Indeed, we
503 would anticipate that the prolonged SynSAC arrest allows for robust chromosomal alignment
504 and minimal requirement for Ipl1$^{Aurora\ B}$-dependent error-correction. We previously found that,
505 globally, Cdc5^{Polo} kinase promotes phosphorylation of a more stringent motif of [DEN]x[ST]*F
506 specifically in meiotic metaphase I (Koch et al., 2024). We found that this trend also applies
507 to kinetochores since the number of phosphorylation sites on kinetochore proteins that match
508 this motif was also highest at metaphase I (Figure 9B). Finally, there was no stage-specific
509 enrichment of the motif recognised by the DDK kinase Cdc7, known to function in DNA
510 damage repair and homologous recombination in prophase (Figure 9B), suggesting that its
511 activity is widespread through mitosis and meiosis, or that other kinases can recognise these
512 sites.
513 Given that the minimal Cdk and Cdc5^{Polo} kinase motifs were common among
514 kinetochore phospho-sites, we also analysed whether these sites were preferentially located
515 within specific sub-complexes. For Cdc5^{Polo} motif sites, this revealed a slight enrichment within
516 the outer kinetochore complexes KMN and Dam1c compared with the inner kinetochore
517 CCAN sub-complex, and this trend was most prominent at metaphase II and mitosis (Figure
518 9C). Conversely, at all stages there was an enrichment for Cdk motif sites within the inner
519 kinetochore CCAN complex vs the outer kinetochore KMN and Dam1 sub-complexes. Finally,

520 we reveal the identities of individual Cdc5^{Polo} and Cdk motif phospho-sites across the core
521 kinetochore (Figure 9D). There was a range of different trends, with some sites being
522 phosphorylated relatively equally across stages while others appeared enriched at specific
523 stages. Together, this dataset provides a strong basis for identifying phosphorylation sites
524 which may have key stage-specific roles such as directing mono-orientation in meiosis I and
525 biorientation in meiosis II.
526
527 **Discussion**
528 Mitosis, meiosis I and meiosis II involve distinct segregation events, each with specific
529 modifications to chromosome structure and orientation that must function in the context of a
530 unique cell cycle programme. Understanding these changes biochemically relies on the ability
531 to harvest cells at these distinct cell cycle stages for direct comparisons. Until now, meiosis II
532 has been particularly elusive since robust methods to arrest budding yeast cells in this stage
533 been lacking. However, meiosis II is of key interest: although it is often referred to as
534 "resembling mitosis", there are crucial differences since it occurs directly after another M
535 phase, meiosis I, and is followed by gamete formation. Here, we developed the SynSAC
536 system to overcome this limitation. SynSAC uses the same yeast strain to arrest cells in
537 metaphase of mitosis, meiosis I or meiosis II, allowing direct comparisons. This system could
538 be applied to interrogate changes in any cellular process or protein complex at these distinct
539 cell cycle stages. Here, as proof of principle, we determined the changes in protein
540 composition and phosphorylation abundance at kinetochores. Our findings develop a new tool
541 for meiotic investigations, provide key insights into meiotic regulation by SAC activation and
542 additionally generate an important resource that provides key insight into how kinetochores
543 are adapted at different cell cycle stages.
544
545 ***A simple method to arrest yeast cells at metaphase II***
546 We found that inducible dimerization of fragments of Spc105 and Mps1 upon prophase
547 release or during anaphase I allows for robust synchronization at metaphase I or II of meiosis,
548 respectively (Figure 1). Since the meiotic SynSAC method relies on two drug-inducible events
549 and does not require media washout steps, it greatly simplifies and improves recovery of
550 metaphase cells. One advantage of SynSAC is that it does not require kinetochore
551 peturbation, as the checkpoint signal is generated ectopically. Since endogenous SAC
552 proteins are also present, SynSAC strains can also mount a response to kinetochore
553 perturbation, as normal. In addition, SynSAC is conditional, allowing the arrest to be induced
554 only at the desired time. This is in contrast to previous studies which have isolated metaphase

555 I cells through repressing transcription of *CDC20* (Lee and Amon, 2003), where loss of the
556 Cdc20 protein, itself part of the mitotic checkpoint complex (McAinsh and Kops, 2023), may
557 have secondary effects. Thus, by relying on relatively quick chemical reactions and achieving
558 arrest without reducing protein levels, the SynSAC method may more accurately reflect the
559 metaphase state. A limitation of this approach, as with any synchronisation system, is that
560 unintended consequences of rewiring cell cycle control cannot be excluded. In the case of
561 SynSAC, such effects could arise from sustained Bub1 signalling, from ectopic activation of
562 the checkpoint away from kinetochores or from induction of enhanced Mps1 activity. Key
563 findings should therefore be validated using orthogonal approaches.
564
565 ***The duration of SAC signalling in metaphase I is regulated by PP1***
566 Interestingly, the duration of SynSAC-mediated delay is consistently shorter in meiosis I vs II,
567 despite equivalent protein level of the dimerizing construct. Microtubule-depolymerising drugs
568 also cause a shorter SAC delay in meiosis I compared to either meiosis II or mitosis
569 (MacKenzie et al., 2023). The differential sensitivity of cells to SynSAC in meiosis I and II
570 suggests that this is an intrinsic difference between the two divisions. Previous work has
571 established a role for PP1 in prematurely silencing the SAC in meiosis I in the presence of
572 improperly attached kinetochores (MacKenzie et al., 2023). Our work similarly implicates PP1
573 binding to Spc105 as being responsible for limiting the duration of the SynSAC arrest in
574 meiosis I. We discovered that mutation of either the conserved RVxF or the GILK motif does
575 indeed lengthen the duration of the metaphase I SynSAC arrest, with the strongest effect seen
576 when both mutations are present. This suggests that PP1 binding to these motifs may promote
577 Spc105 dephosphorylation and SAC silencing in metaphase I. Consistently, PP1 phosphatase
578 Glc7 and its regulatory subunit Fin1, were enriched on meiotic kinetochores (Figure 7A). In
579 contrast, we observed only minor additional delays in metaphase II when PP1 binding to
580 Spc105 was prevented. Moreover, surprisingly, the RASA mutation, but not 4A or 4A RASA
581 abolished the growth defect of SynSAC cells in mitosis. While this finding remains
582 unexplained, it points to differential wiring of checkpoint activation and silencing mechanisms
583 in mitosis, meiosis I and meiosis II. Together, these observations suggest that PP1 activity is
584 more prominent at metaphase I. How this relates to the unique segregation pattern in this
585 division where homologs, rather than sister chromatids, are segregated is an important area
586 of investigation for the future.
587 Previous studies in *S. cerevisiae* found no evidence that Aurora B–dependent
588 phosphorylation of S77 within the RVSF motif inhibits PP1 binding (Rosenberg et al., 2011;
589 Roy et al., 2019), unlike the mechanism described in human cells (Liu et al., 2010). In contrast,

590 we found that the RVAF mutation partially restores mitotic growth in the SynSAC strain and
591 shortens the SynSAC-induced delay in metaphase I. These observations suggest that PP1
592 binding may nevertheless be regulated by phosphorylation within the RVSF motif to attenuate
593 checkpoint signalling, a mechanism that may be particularly important during meiosis I.
594 Interestingly, similar to PP1, CPC subunits, including Ipl1^{AuroraB}, and SAC proteins are enriched
595 on kinetochores in metaphase I. We suggest that the physical linkage of homologs by
596 chiasmata in meiosis I creates additional constraints on biorientation, thereby necessitating
597 repeated error correction through opposing CPC/Aurora B and PP1 activity.
598 Finally, the stronger and more prolonged SynSAC arrest obtained using the PP1
599 binding site mutant *spc105$^{1-455}$-4A-RASA* prompts its consideration as an alternative tool for
600 future studies, particularly where meiosis I arrest is important. At the time of performing the
601 kinetochore immunoprecipitations, these mutations were not yet available but, as we have
602 demonstrated, wild type SynSAC protein fragments nevertheless yielded sufficiently enriched
603 populations of metaphase I and II cells to allow reliable detection of stage-specific kinetochore
604 proteins and phosphorylations. Going forward, however, we consider SynSAC-4A-RASA to
605 be the optimal tool for inducing metaphase arrests.
606
607 ***Kinetochore composition dynamics in meiosis reveal distinct functional states***
608 We applied SynSAC to understand changes in composition of the kinetochore by quantitative
609 proteomic analysis. Prior work used Dsn1 kinetochore immunoprecipitations and
610 minichromosome purifications to compare kinetochore and centromere composition in mitosis,
611 prophase I and metaphase I (Borek et al., 2021). However, analysis of purified metaphase II
612 kinetochores was previously inaccessible and our application of high-sensitivity DIA mass
613 spectrometry, together with matched phosphorylation analysis, provides a more complete
614 picture overall. Our dataset of kinetochore composition from four stages: (1) mitotic
615 metaphase I; (2) meiotic prophase I; (3) metaphase I and (4) metaphase II therefore greatly
616 extends our understanding of how kinetochores change during meiosis. Consistent with
617 remodelling reported in our earlier study (Borek et al., 2021), we reveal a change in the
618 stoichiometry of sub-complexes relative to each other, dependent on cell cycle stage. For
619 example, the inner kinetochore CCAN is less abundant at meiotic metaphase I and II
620 compared with mitosis and prophase (Figure 7A). The mechanisms underlying the lower
621 abundance of CCAN proteins, which notably include some of the most essential DNA-
622 contacting proteins such as the Cse4^{CENP-A} histone and the Ame1^{CENP-C}/Okp1^{CENP-Q}
623 heterodimer, during meiotic metaphase require further investigation. Moreover, it is possible
624 that this phenomenon contributes to the essential requirement for some CCAN proteins for

625 kinetochore assembly in meiosis, but not mitosis (Borek et al., 2021; Fernius and Marston,
626 2009; Mehta et al., 2014). Conversely, we observed higher levels of Dam1 complex proteins
627 at meiotic metaphase I and II compared with mitosis, and this trend was significant for the
628 complex as a whole (Figure 7A-B). Along the same lines, there was a small but statistically
629 significant increase in the levels of KMN proteins in metaphase I specifically (Figure 7A-B).
630 Overall, there is a trend for a loss in inner kinetochore protein interactions and a gain in outer
631 kinetochore protein interactions in meiotic metaphase compared to mitotic metaphase.
632 Although some variation could reflect global changes in protein abundance during meiosis,
633 we previously found that only a few proteins undergo dynamic abundance changes during the
634 meiotic divisions (Koch et al., 2024), so this is unlikely to fully explain the kinetochore
635 composition differences observed. Instead, it is tempting to speculate that kinetochores are
636 more loosely associated with chromatin and more strongly associated with the spindle through
637 the outer kinetochore in meiotic vs mitotic metaphase. Potentially, kinetochore-spindle
638 interactions are stabilised to better ensure accurate segregation during the rapid metaphase-
639 anaphase transitions of meiosis and to cope with the challenging configuration of homologs in
640 meiosis I, relying on chiasmata-dependent linkages.

641 Our data also provide insight into the unique regulatory state of meiosis I kinetochores.
642 Consistent with our previous findings (Borek et al., 2021), meiotic axis (Red1) and
643 synaptonemal complex protines (Zip1) are enriched on prophase kinetochores and the
644 meiosis I-specific monopolin complex was enriched on metaphase I kinetochores. Cohesins
645 (Smc1 and Smc3) were also enriched on metaphase I kinetochores, supporting the
646 requirement for a dedicated pool of centromeric cohesion for mono-orientation at this stage
647 (Barton et al., 2022). Casein kinase 1 (CK1/Hrr25), which plays multiple roles in meiosis,
648 including as a component of monopolin (Argüello-Miranda et al., 2017; Galander et al., 2019;
649 Petronczki et al., 2006), was immunoprecipitated with kinetochores at all meiotic stages. As
650 noted above, PP1 phosphatase and CPC-Aurora B kinase enrichment further suggest
651 dynamic phospho-regulation in metaphase I consistent with our detection of increased
652 kinetochore-associated phosphorylations at this stage compared to metaphase II or mitosis
653 (Figure 8A). Furthermore, the pericentromeric cohesin protector, shugoshin (Sgo1), was
654 highly enriched on metaphase I compared to metaphase II kinetochores. This is consistent
655 with recent work in mouse oocytes which indicated that shugoshin-dependent cohesin
656 protection is lost prior to meiosis II (El Jailani et al., 2025). Nevertheless, imaging experiments
657 show that shugoshins are retained at meiosis II kinetochores (Galander et al., 2019; Katis et
658 al., 2004; Marston et al., 2004; Mengoli et al., 2021), albeit at a reduced level, suggesting that
659 they may play additional roles in meiosis II. Overall, these findings indicate dynamic changes

660 in the composition of kinetochore-associated proteins during meiosis and provide a starting
661 point for future studies directed at their functional significance.
662
663 ***Metaphase II kinetochores have reduced phosphorylation***
664 Our phospho-proteomic analysis of purified kinetochores from meiosis and mitosis identified
665 4,487 phosphorylation sites on 1,614 proteins, indicating that ~35% of the detected proteome
666 is phosphorylated, in agreement with previous studies (Figure 8-figure supplement 1A)
667 (Ptacek et al., 2005; Wettstein et al., 2024). Nearly twice as many phospho-sites were
668 identified in meiotic prophase and metaphase I compared with metaphase II and mitotic
669 metaphase (Figure 8-figure supplement 1A). Around 250-400 more proteins were detected in
670 prophase and metaphase I, suggesting unique regulation at the level of protein abundances
671 as well as phosphorylation (Figure 5-figure supplement 2A). We found less variation in the
672 number of phospho-sites found on known kinetochore proteins, with around 100 sites
673 identified on ~70 kinetochore proteins across all stages (Figure 8A). Despite this similarity, we
674 quantified significant differences in the overall abundances of the phospho-sites, with meiotic
675 prophase and metaphase I kinetochores having significantly higher levels of phosphorylation
676 compared with meiotic metaphase II and mitotic metaphase (Figure 8A). Within the core
677 kinetochore structure, most phospho-sites mapped to the chromatin-associated CCAN or the
678 spindle-associated KMN complexes. Around 40% of CCAN phosphosites matched the CDK
679 consensus, suggesting that CDK control of kinetochore assembly timing may be concentrated
680 at the inner kinetochore. It is also interesting that the two most dynamic phosphoproteins
681 identified in our study, Dsn1 and Mif2^{CENP-C} (Figure 8C), are implicated in recruitment of factors
682 required for the unique mono-oriented arrangement of sister chromatids in meiosis I. An N-
683 terminal extension on Dsn1 directly binds monopolin (Plowman et al., 2019; Sarkar et al.,
684 2013), while mouse and fission yeast CENP-C recruit MOKIRs Moa1 and Meikin (Kim et al.,
685 2015; Tanaka et al., 2009). It therefore seems highly likely that some of the stage-specific
686 phosphorylation events are important for regulating the switch in kinetochore orientation in
687 meiosis, and future research should aim for their functional characterisation.
688 Furthermore, most of the detected phosphorylation sites were unique to the stage and
689 therefore their function is likely to be stage-specific (Figure 8-figure supplement 1B). Whether
690 sister kinetochore biorientation at metaphase II and mitotic metaphase is physically and/or
691 biochemically distinct remains unclear. Our characterisation of meiotic SynSAC duration and
692 previous work with the endogenous SAC (MacKenzie et al., 2023) suggest that metaphase II
693 is regulated differently, with metaphase II having a shorter arrest compared to mitotic
694 metaphase upon SynSAC activation. However, previous biophysical characterisation

695 indicated that the kinetochore-microtubule attachment strength of metaphase II and mitotic
696 purified kinetochores was equivalent on average (Sarangapani et al., 2014). Thus, it may be
697 that the shorter duration of metaphase II does not depend on maximum attachment strength
698 per se and rather on some intrinsic cell cycle regulation or other properties of kinetochores in
699 these stages. Indeed, the distance between sister centromeres in mouse metaphase II
700 oocytes is nearly double that in human and mouse mitotic cells, so there are likely biophysical
701 differences between biorientation at these two stages (Kouznetsova et al., 2019). Additionally,
702 as many as ~20% of chromosomes in mouse metaphase II cells appear to have lateral or
703 merotelic attachments that persist into anaphase II, when they are then corrected
704 (Kouznetsova et al., 2019). Thus, compared with mitosis, error-correction mechanisms are
705 notably different in meiosis. Error-correction relies on phospho-regulation of the outer
706 kinetochore sub-complexes KMN and Dam1c, and we observed higher levels of Dam1
707 complex proteins in kinetochores from meiosis vs mitosis. This, in addition to the differential
708 phospho-sites identified on outer kinetochore proteins, provides a good first step for future
709 investigations into meiotic kinetochore attachment mechanisms and how they differ in meiosis
710 I and meiosis II.
711
712
713 **Materials and Methods**
714
715 ***Plasmids***
716 Plasmids used in this study are listed in Supplemental Table 1.
717 *MPS1(440-765)* in a *HIS3* single integration plasmid AMp1725 was made by restriction
718 digest of empty *HIS3* single integration plasmid AMp1694 (received from Biggins Lab) and
719 *MPS1(440-765)* amplified from wild type SK1 yeast genomic DNA. *pMPS1-MPS1(440-765)* in
720 a *HIS3* single integration plasmid AMp1740 was made by Gibson assembly of ~500bp of
721 *MPS1* promoter amplified from wild type SK1 yeast genomic DNA and AMp1725. *pMPS1-*
722 *MPS1(440-765)-AB*I in a *HIS3* single integration plasmid AMp1755 was made by Gibson
723 assembly of ABI amplified from AMp1460 (received from Hardwick Lab, made in Heun Lab)
724 and AMp1740.
725 *pSPC105-SPC105(1-455)-PYL-3FLAG* in a *LEU2* single integration plasmid AMp1741
726 was made by Gibson assembly of 3 parts. ~500bp of *SPC105* promoter and *SPC105(1-455)*
727 were amplified from wild type SK1 genomic DNA, *PYL-3FLAG* was amplified from plasmid
728 AMp1461 (received from Hardwick Lab, made in Heun Lab) and *LEU2* single integration
729 plasmid AMp1697 (received from Biggins Lab).

730 *pSPC105-SPC105(1-455)-PYL* in a *LEU2* single integration plasmid AMp2055 was
731 made by megaprimer mutagenesis (two-step PCR) to completely remove the 3FLAG tag in
732 AMp1741.
733 PP1 binding site mutations in *SPC105-PYL* plasmids were made by megaprimer
734 mutagenesis. *spc105(1-455)-4A* mutates the 21-GILK-24 motif to 21-AAAA-24. *spc105(1-*
735 *455)-RASA* mutates the 75-RVSF-78 motif to 75-RASA-78. The *spc105(1-455)-4A-RASA*
736 plasmid contains both sets of mutations. *spc105(1-455)-RVAF* mutates serine 77 to alanine
737 only.
738
739 ***Yeast strains***
740 Budding yeast strains used in this study were derivatives of SK1 and are listed in
741 Supplemental Table 2. *pGAL1-NDT80 pGPD1-GAL4.ER* was described previously (Benjamin
742 et al., 2003). The *MPS1-3V5*, *SPC105-6His-3Flag*, and *DSN1-6His-3Flag* strains were made
743 by standard PCR tagging methods. SynSAC strains with *MPS1(440-765)-ABI* and *SPC105(1-*
744 *455)-PYL* integrated at the *his3* and *leu2* locus, respectively, were made by restriction
745 digestion of the appropriate plasmids and standard yeast DNA transformation procedures.
746 Yeast strains are available upon request without restriction.
747
748 ***Meiotic prophase block-release timecourse***
749 Cells were induced to undergo meiosis as described by (Barton et al., 2022) and *pGAL-*
750 *NDT80* prophase block-release experiments were performed as outlined in (Carlile and Amon,
751 2008). Briefly, strains were patched from –80 °C stocks to YPG agar (1% Bacto yeast extract,
752 2% Bacto peptone, 2.5% glycerol, 0.3 mM adenine, 2% agar) plates. After ~16 h, cells were
753 inoculated into YPDA media and grown for 24 h at 30 °C with shaking at 250 rpm. Next,
754 BYTA (1% Bacto yeast extract, 2% Bacto tryptone, 1% potassium acetate, 50 mM potassium
755 phthalate) cultures were prepared to OD_{600} = 0.3 and grown at 30 °C with shaking at 250 rpm
756 overnight (~16 h). The next morning, cells were washed twice in sterile water and resuspended
757 in sporulation medium (0.3% potassium acetate, pH=7.0) at OD_{600} = 2.0. After 5.5 h in
758 sporulation media, 1 µM β-estradiol was added to release cells from prophase and samples
759 were collected for immunofluorescence every 15 min until 180 min, and then every 30 min for
760 a further hour. For experiments where protein samples were analysed by Western blotting, 10
761 ml of meiotic culture or 5 ml of mitotic culture was collected by centrifugation and resuspended
762 in 5 ml ice-cold 5% trichloroacetic acid (TCA). Cells were collected again by centrifugation and
763 transferred to Fastprep (MP) tubes. Cell pellets were snap frozen in liquid nitrogen and stored
764 at -70 °C. Frozen cell pellets were washed in 500 µl acetone and air-dried. Cell pellets were

765 resuspended in TE with 2.75µM DTT and 1x Roche cOmplete protease inhibitor cocktail.
766 Protein samples were prepared by bead-beating in an MP Fastprep machine, at speed 6.5 for
767 3 rounds of 45 seconds with 1 min on ice in between, at 4 °C. SDS Sample buffer was added
768 (final concentration 3% SDS) and samples were boiled for 3 minutes before PAGE.
769
770 ***Spore viability assay***
771 All spore viability assays were carried out following prophase block-release timecourses.
772 Following the timecourse, cultures were left shaking at 30 °C ~24h. 100ul of culture was
773 collected by spinning in a microcentrifuge for 1min 13k rpm and then resuspended in 20ul
774 1mg/ml zymolyase in 1M sorbitol and incubated for 10 minutes at room temperature before
775 adding 1mL sterile water. Tetrads were dissected with a micromanipulator on a Nikon Eclipse
776 50i light microscope.
777
778 ***Mitotic alpha factor arrest-release timecourse***
779 Yeast strains were patched from –80 °C stocks to YPG agar (1% Bacto yeast extract, 2%
780 Bacto peptone, 2.5% glycerol, 0.3 mM adenine, 2% agar) plates. The next day, strains were
781 patched to YPDA (1% Bacto yeast extract, 2% Bacto peptone, 2% glucose, 0.3mM adenine)
782 agar plates. The next day, cells were inoculated into YPDA medium and grown overnight ~16h
783 at 30 °C with shaking at 250 rpm. The next morning, cultures were diluted to OD ~0.2 and
784 grown for 2 hours at room temperature with shaking at 250 rpm. Cultures were diluted back
785 to OD ~0.2 and alpha factor was added to 7.5 µg/ml. Cultures were shaken at room
786 temperature for 3 hours before checking that >90% of cells were shmooing or unbudded. Cells
787 were washed three times in 2x volume water and collected by centrifuging in a tabletop
788 centrifuge 3k rpm for 2 minutes at room temperature. Cells were resuspended in fresh YPDA
789 and placed into clean flasks. Culture samples of 100µl were taken at time zero before addition
790 of either ethanol or 250 µM abscisic acid (ABA) and then at 30 minute intervals after addition
791 of ethanol or ABA. 100ul culture samples were immediately combined with 400µl ethanol and
792 stored at 4 °C. For DNA staining, cells were pelleted and resuspended in 100ul 1 µg/ml DAPI
793 in PBS. Yeast cells were sonicated for 30 seconds on low in a Bioruptor Twin sonicating device
794 (Diagenode) and glass slides were prepared and visualised on a Zeiss Axioplan Imager Z2
795 fluorescence microscope with a 100x Plan ApoChromat NA 1.45 oil lens. At least 100 cells
796 were counted for each condition.
797
798 ***Serial dilution mitotic growth assay***

799 Yeast strains were inoculated into YPDA medium and grown overnight ~16h at room
800 temperature. Cultures were diluted to OD_{600}=0.2 and grown to mid-log at room temperature
801 before being diluted back to OD_{600}=0.3. Serial dilutions were set up in 96-well plates, with 5-
802 fold dilutions across rows. Yeast were transferred to YPDA plates or YPDA plates spread with
803 250 µM abscisic acid (ABA). Plates were incubated at 30 °C for ~24 h before taking images.
804
805 ***Spindle immunofluorescence***
806 Meiotic spindles were visualised by indirect immunofluorescence as described in (Barton et
807 al., 2022). A rat anti-tubulin primary antibody (AbD serotec) at 1:50 dilution and an anti-rat
808 FITC conjugated secondary antibody (Jackson Immunoresearch) at 1:100 dilution were used.
809 A Ziess Axioplan Imager Z2 fluorescence microscope with a 100x Plan ApoChromat NA 1.45
810 oil lens was used to visualise cells. In total, 100-200 cells were counted at each timepoint
811 and/or for each sample.
812
813 ***SDS-PAGE and Western blotting***
814 SDS-PAGE and Western blotting were carried out largely as described in (Barton et al., 2022),
815 with minor modifications. Protein samples were separated on 10% bis-tris acrylamide gels
816 submerged in running buffer (25 mM Tris, 190 mM glycine, 0.01% SDS) using the Bio-Rad
817 Mini-Protean or Scie-plas TV200Y wide format mini gel system. SDS-PAGE gels were
818 transferred onto nitrocellulose membrane (0.45uM, Amersham-GE Healthcare) in transfer
819 buffer (25 mM Tris, 1.5% glycine, 0.02% SDS, 10% methanol) in a Bio-Rad Mini Trans-Blot
820 system or a semi-dry Amersham TE70 transfer unit.
821 Membranes were blocked in 5% milk in PBS with 0.01% Tween-20 (PBST) for at least
822 30 minutes before incubation in primary antibody overnight with gentle shaking at 4 °C. At
823 room temperature, membranes were washed three times for 10 minutes in PBST before
824 incubation in secondary antibody for 1 hour. Membranes were washed for 10 minutes, 3 times,
825 before visualisation using chemiluminescence. HRP-conjugated antibodies were detected
826 with ECL blotting substrate (Pierce), SuperSignal West Pico Plus substrate (Pierce), or
827 SuperSignal West Atto substrate (Pierce) for weaker signals and images were acquired with
828 a ChemiDoc MP Imaging System (Bio-Rad).
829
830 ***Growth conditions for kinetochore immunoprecipitations***
831 All immunoprecipitations were performed with lysate from either a *DSN1-His-Flag*
832 strain (33675) or no tag *DSN1* (30990) strain grown in different conditions.

833 For each replicate from meiotic cultures, two cultures of 400mL OD~2.0 were
834 sporulated in 4L flasks and scored for metaphase arrest by spindle IF as appropriate. Cultures
835 that were most similar by date of growth and spindle IF were combined during later grinding
836 lysis. For each replicate from mitotic cultures, 800ml OD=1.1-1.3 culture was grown in one 4L
837 flask and harvested and processed together.
838 For each 400mL meiotic culture, strains were patched from -70 stocks to YPG plates
839 and grown at 30C. After ~24h, a 25mL YPDA culture in a 250 mL flask was inoculated and
840 grown at 30C, shaking at 250 rpm. After ~24h, a 200mL BYTA culture in a 2L flask was started
841 at OD=0.2 and grown at 30C, shaking at 250rpm. The next morning, after ~16h, a 400ml
842 culture in a 4L flask was started at OD~2.0 in sporulation medium. All meiotic cultures were
843 grown at 30C with shaking at 250rpm. For meiotic prophase, cultures were incubated for 5.5
844 hours before harvest. For metaphase I, cultures were incubated for 5.5 hours before 1 µM β-
845 estradiol and 250uM ABA were added together. After 90 minutes, cells were harvested. For
846 metaphase II, cultures were incubated for 5.5 hours before 1 µM β-estradiol was added. After
847 105 minutes, 250 µM ABA was added and cells were harvested at 135 minutes. Samples for
848 spindle immunofluorescence were collected at the time of harvest.
849 For each mitotic culture, strains were patched from -70 stocks to YPG plates and grown
850 at 30C. After ~24h, a 25mL YPDA culture was inoculated in a 125mL flask and grown at 30C
851 with shaking at 250rpm. After ~16h, an 800 mL YPDA culture was started in a 4L flask at
852 OD~0.3 and grown at 30C with shaking at 250rpm. After ~3h, the OD=1.1-1.2 culture was
853 harvested.
854
855 ***Immunoprecipitation of kinetochores for mass spectrometry***
856 Immunoprecipitations were carried out essentially as described in (Borek et al., 2021),
857 with minor modifications.
858 *Harvest:* Cell cultures were spun at 4k rpm for 5 min at 4C in a Beckman Avanti J25
859 centrifuge. Each 400ml cell culture pellet was washed in 150 mL water and spun again the
860 same way. Then, cell pellets were resuspended in BH0.15 lysis buffer (150mM KCl, 25mM
861 HEPES-KOH pH 8.0, 2mM MgCl2, 0.5mM EGTA-KOH pH 8.0, 0.1mM EDTA-KOH pH 8.0,
862 0.1% NP-40) including phosphatase inhibitors (5mM NaF, 2mM Na-beta-glycerophosphate,
863 1mM sodium pyrophosphate, 800uM sodium orthovanadate, 200nM microcystin-LR) and
864 protease inhibitors (2mM Pefabloc, 10ug/ml each of 'CLAAPE' (Chymostatin,
865 Leupeptin,Aprotinin,Antipain,Peptstatin A,E-64), and 1x Roche cOmplete inhibitor cocktail).
866 Cell pellets were resuspended in BH0.15 including inhibitors according to the following
867 equation: OD600 x culture volume in L x 2 = mL buffer (ie for each 400 mL OD=2.0 pellet,

868 cells were resuspended in 1.6mL buffer). Resuspended cultures were drop frozen into liquid
869 nitrogen and stored at -70 before further processing.
870 *Lysis:* Frozen cell pellets were lysed by cryo-grinding in a SPEX 6875 Freezer Mill,
871 with 5 min pre-cool, 2 min Run time, 2 min Cool time, 8 cycles of 10 cycles per second. Cryo-
872 grindate was stored at -70 before further processing.
873 *Antibody conjugation to Dynabeads:* As described in (Borek et al., 2021). Antibody-
874 conjugated Protein G Dynabeads (ThermoFisher) were always prepared no more than 24
875 hours before use and were stored at 4 C until use.
876 *Immunoprecipitation and elution:* Grindate powder, in 50mL falcons, was thawed in
877 room temperature water before transferring to ice. Thawed grindate was clarified by
878 centrifugation in a tabletop centrifuge at 3,500 rpm for 10 min 4C. The supernatant, the lysate,
879 was transferred to a new falcon tube and concentration measured by standard Bradford Assay
880 (BioRad Cat#5000006). IPs were set up so that 80-100mg protein was incubated with ~100
881 uL anti-FLAG conjugated Protein G Dynabeads (ThermoFisher). The ratio of protein to beads
882 was always kept such that 12.6 mg protein was incubated with 15 uL antibody-conjugated
883 beads. IPs of replicates of the same condition were all done on the same day and normalised
884 so that protein concentration and antibody-bead volumes were the same between replicates.
885 Protein lysates and antibody-conjugated Dynabeads were incubated together in falcon tubes
886 with gentle rotation at 4C for 3 hours. Next, supernatants were collected and beads were
887 washed twice in 1mL BH0.15 with phosphatase and protease inhibitors by gently inverting the
888 tubes, then washed once in 1mL BH0.15 alone. Protein was eluted from beads in two rounds
889 of 10 min at 50C in a ThermoMixer C (Eppendorf) at 500-600 rpm with 0.1% RapiGest SF in
890 50mM Tris pH 8.0, added to one-half volume of Dynabeads (ie two rounds of 50 ul elution for
891 100 ul Dynabeads). The two sequential elutions were combined and the eluate was stored at
892 -70 before further processing.
893
894 ***Silver staining***
895 Protein samples were separated on 4-12% NuPAGE pre-cast gels (Invitrogen) run in MES
896 buffer (50mM MES, 50mM Tris Base, 0.1% SDS, 1mM EDTA, pH 7.3) and stained using an
897 Invitrogen Silverquest staining kit following the manufacturer's instructions.
898
899 ***Preparation of samples for mass spectrometry***
900 RapiGest eluates were prepared for mass spectrometry by trypsin digestion with a
901 filter-aided sample preparation (FASP) method, essentially as described in (Koch et al., 2024;
902 Wiśniewski et al., 2009).

903

904 ***Phospho-peptide enrichment***

905 For each trypsin-digested peptide solution, 5% was loaded directly onto C18 stage
906 tips, called the "N" sample, and 95% was processed for phospho-peptide enrichment via Ti-
907 IMAC beads (MagReSyn) as described in (Koch et al., 2024), and called the "PE" (for
908 phospho-enriched) sample before loading on C18 stage tips. Samples of the same condition
909 were all processed on the same day (eg all prophase samples were processed together on
910 the same day).

911

912 ***DIA mass spectrometry***

913 The "N" and "PE" peptides eluted from the filter units were acidified using 20 μl of 10%
914 Trifluoroacetic Acid (TFA) (Sigma Aldrich). Samples were spun onto StageTips as described
915 by (Rappsilber et al., 2007). Peptides were eluted in 40 µL of 80% acetonitrile in 0.1% TFA
916 and concentrated down to 1 µL by vacuum centrifugation (Concentrator 5301, Eppendorf, UK).
917 They were then prepared for LC-MS/MS analysis by diluting it to 5 µL by 0.1% TFA.

918 LC-MS analyses were performed on Orbitrap Exploris™ 480 (Thermo Fisher Scientific,
919 UK) on a Data Independent Acquisition (DIA) mode, coupled on-line, to an Ultimate 3000
920 HPLC (Dionex, Thermo Fisher Scientific, UK). Peptides were separated on a 50 cm (2 μm
921 particle size) EASY-Spray column (Thermo Scientific, UK), which was assembled on an
922 EASY-Spray source (Thermo Scientific, UK) and operated constantly at 55°C. Mobile phase
923 A consisted of 0.1% formic acid in LC-MS grade water and mobile phase B consisted of 80%
924 acetonitrile and 0.1% formic acid. Peptides were loaded onto the column at a flow rate of 0.3
925 µL min^{-1} and eluted at a flow rate of 0.25 µL min^{-1} according to the following gradient: 2 to 40%
926 mobile phase B in 150 min and then to 95% in 11 min. Mobile phase B was retained at 95%
927 for 5 min and returned back to 2% a minute after until the end of the run (160 min).

928 Survey scans were recorded at 120,000 resolution (scan range 350-1650 m/z) with an
929 ion target of 5.0e6, and injection time of 20ms. MS2 was performed in the orbitrap at 30,000
930 resolution with a scan range of 200-2000 m/z, maximum injection time of 55ms and AGC
931 target of 3.0E6 ions. We used HCD fragmentation with stepped collision energy of 25.5, 27
932 and 30. We used variable isolation windows throughout the scan range ranging from 10.5 to
933 50.5 m/z. Narrow isolation windows (10.5-18.5 m/z) were applied from 400-800 m/z and then
934 gradually increased to 50.5 m/z until the end of the scan range. The default charge state was
935 set to 3. Data for both survey and MS/MS scans were acquired in profile mode.

936

937 ***Mass spectrometry library search conditions***

938 The DIA-NN software platform (Demichev et al., 2020) version 1.9.2. was used to
939 process the DIA raw files and search was conducted against our in house *Saccharomyces*
940 *cerevisiae* complete/reference proteome (original database from Saccharomyces Genome
941 Database for the strain SK1, released in May, 2019). Precursor ion generation was based on
942 the chosen protein database (automatically generated spectral library) with deep-learning
943 based spectra, retention time and IMs prediction. Digestion mode was set to specific with
944 trypsin allowing maximum of two missed cleavages. Carbamidomethylation of cysteine was
945 set as fixed modification. Oxidation of methionine, acetylation of the N-terminus and
946 phosphorylation on serine, threonine and tyrosine were set as variable modifications. The
947 parameters for peptide length range, precursor charge range, precursor m/z range and
948 fragment ion m/z range as well as other software parameters were used with their default
949 values. The precursor FDR was set to 1%. Annotating library proteins were created with
950 information from the FASTA database.
951
952 ***Mass spectrometry data analysis in R***
953 All data analysis was performed using the report.pg_matrix.tsv and
954 report.phosphosites_99.tsv files from DIA-NN version 1.9.2 using R (v 4.2.3) within the
955 RStudio environment.
956 For proteins, the columns corresponding to the measurements of the non-phospho-
957 enriched ("N") samples in the report.pg_matrix.tsv file were analysed. For phospho-sites, the
958 columns corresponding to the measurements of the phospho-enriched ("PE") samples in the
959 report.phosphosites_99.tsv file were analysed. Only phospho-peptides with greater than or
960 equal to 99% localisation confidence for the phospho- modification at the given site residue
961 are included in the measurements in the report.phosphosites_99.tsv file. In DIA-NN, phospho-
962 site abundances can include measurements from multiply-modified peptides, however the
963 vast majority of phospho-sites are quantified from singly phospho-peptides.
964 No imputation was carried out. Due to low coverage, only two out of three replicates
965 of the mitotic DSN1 ("no tag") "N" samples were analysed for protein levels and only two out
966 of three replicates from each of the mitotic DSN1 ("no tag") and mitotic Dsn1-His-Flag ("tag")
967 "PE" samples were analysed for phospho-site abundances. Samples from Dsn1-His-Flag
968 ("tag") IPs and DSN1 ("no tag") IPs were normalised separately. All IP samples of the same
969 type ("tag" or "no tag"), including all replicates and cell cycle stages, were normalised together.
970 For both the protein measurements of the "N" samples and the phospho-site measurements
971 from the "PE" samples, a column median normalisation was carried out; all values in a given
972 sample column were multiplied by a scaling factor consisting of the median intensity of all

973 sample columns divided by the median sample intensity of that individual column. To
974 normalise phospho-site abundances to the protein level, each column-normalised value from
975 the "PE" measurements of the phosphosites_99 file were divided by the corresponding
976 column-normalised protein (from "N") measurement from the pg_matrix table and multiplied
977 by 1000. For example the normalised value of phospho-site Ndc80-T-54 in the PE sample of
978 the phosphosites_99 table was divided by the normalised value of the protein Ndc80 in the
979 corresponding N sample of the pg_matrix and multiplied by 1000.
980 To better analyse differential protein levels between IPs, the protein measurements
981 from the "N" samples were further scaled by the measurement of Dsn1 within each sample.
982 Each normalised protein measurement was divided by the normalised value of Dsn1 within
983 that sample. All protein measurements shown in Figures 6 and 7 are Dsn1-scaled.
984 Protein and phospho-site measurements were further analysed using functions from
985 the Differential Enrichment of Proteins (DEP) R package (Zhang et al., 2018). Both protein
986 and phospho-site tables were filtered to include only proteins or sites that were measured in
987 all replicates of at least one condition.
988 Venn diagrams were made using interactivenn.net (Heberle et al., 2015). For the GO
989 term enrichment analysis, ranked lists were generated. Proteins or phospho-proteins were
990 ranked by descending fold-change and known kinetochore proteins were excluded. For each
991 stage, comparison with the other stages generated three ranked lists. The top 50 proteins
992 from all three lists were combined together in one list and duplicates were removed. Using
993 these lists, GO term enrichment was carried out using gprofiler2 R package (Kolberg et al.,
994 2020) with organism="scerevisiae" and otherwise default settings. For the ranked lists in Supp
995 Fig 6 Supp 2 and Fig 8 Supp 1, proteins were ranked by descending fold-change, known
996 kinetochore proteins were excluded, and the top 20 proteins were selected.
997 The stat_pwc() function from the ggpubr R package was used to run statistical tests
998 comparing protein or phospho-site intensities. For boxplots, a two-sided Wilcoxon test was
999 run and p-values adjusted with the Bonferroni method. For barplots in Figure 8D, a two-sided
1000 t-test was run and p-values adjusted with the Bonferroni method. In all figures, a single
1001 asterisk (*) indicates a p-value of less than 0.05, two asterisks (**) a p-value less than
1002 0.01, and three asterisks (***) p-value of less than 0.001.
1003 The ggseqlogo R package was used to make phospho-site motif logos (Wagih, 2017).
1004
1005 **Data Availability**
1006 Mass spectrometry data generated in this study has been deposited at the PRIDE database
1007 with dataset identifier PXD067911.

The R script for all data analysis in this study is provided as Source Code 1 and published on Github (https://github.com/lori-koch/Kinetochore-SynSAC).

Acknowledgements

We are grateful to Sue Biggins, Kevin Hardwick and Patrick Heun for plasmids, to Marina Altamirano De Castro for assistance with plasmid and strain construction, and to Flora Paldi for initial exploratory experiments for induction of metaphase II arrest. We thank Kevin Hardwick and all members of the Marston group for helpful discussions. We gratefully acknowledge the Wellcome Discovery Research Platform for Hidden Cell Biology Proteomics Core for mass spectrometry support. This work was funded through a Wellcome Investigator award to ALM [220780], a Wellcome Multi-User Equipment Grant [218305], core funding for the Wellcome Centre for Cell Biology [203149] and a Wellcome Discovery Research Platform Award [226791].

Author contributions

Conceptualization – LK and AM; Data curation –LK and CS; Funding Acquisition – AM; Formal Analysis – LK, TG, and CS; Investigation – LK and TG; Software – LK; Supervision –AM; Visualization – LK and AM; Writing – original draft – LK; Writing – review and editing – LK and AM with input from all authors

Disclosure and competing interests statement

The authors declare no conflicts of interest.

References

Akiyoshi B, Nelson CR, Ranish JA, Biggins S. 2009. Analysis of Ipl1-mediated phosphorylation of the Ndc80 kinetochore protein in Saccharomyces cerevisiae. Genetics **183**:1591–1595. DOI: https://doi.org/10.1534/genetics.109.109041, PMID: 19822728

Akiyoshi B, Sarangapani KK, Powers AF, Nelson CR, Reichow SL, Arellano-Santoyo H, Gonen T, Ranish JA, Asbury CL, Biggins S. 2010. Tension directly stabilizes reconstituted kinetochore-microtubule attachments. Nature **468**:576–579. DOI: https://doi.org/10.1038/nature09594, PMID: 21107429

Amin P, Soper Ní Chafraidh S, Leontiou I, Hardwick KG. 2018. Regulated reconstitution of spindle checkpoint arrest and silencing through chemically induced dimerisation in vivo. Journal of Cell Science **132**:jcs219766. DOI: https://doi.org/10.1242/jcs.219766, PMID: 30237224

Araki Y, Gombos L, Migueleti SPS, Sivashanmugam L, Antony C, Schiebel E. 2010. N-terminal regions of Mps1 kinase determine functional bifurcation. The Journal of Cell Biology **189**:41–56. DOI: https://doi.org/10.1083/jcb.200910027, PMID: 20368617

Aravamudhan P, Goldfarb AA, Joglekar AP. 2015. The kinetochore encodes a mechanical switch to disrupt spindle assembly checkpoint signalling. Nature Cell Biology **17**:868–879. DOI: https://doi.org/10.1038/ncb3179, PMID: 26053220

Argüello-Miranda O, Zagoriy I, Mengoli V, Rojas J, Jonak K, Oz T, Graf P, Zachariae W. 2017. Casein Kinase 1 Coordinates Cohesin Cleavage, Gametogenesis, and Exit from M Phase in Meiosis II. Developmental Cell **40**:37–52. DOI: https://doi.org/10.1016/j.devcel.2016.11.021, PMID: 28017619

Barton RE, Massari LF, Robertson D, Marston AL. 2022. Eco1-dependent cohesin acetylation anchors chromatin loops and cohesion to define functional meiotic chromosome domains. eLife **11**:e74447. DOI: https://doi.org/10.7554/eLife.74447, PMID: 35103590

Benjamin KR, Zhang C, Shokat KM, Herskowitz I. 2003. Control of landmark events in meiosis by the CDK Cdc28 and the meiosis-specific kinase Ime2. Genes & development **17**:1524–1539.

Berchowitz LE, Gajadhar AS, van Werven FJ, De Rosa AA, Samoylova ML, Brar GA, Xu Y, Xiao C, Futcher B, Weissman JS, White FM, Amon A. 2013. A developmentally regulated translational control pathway establishes the meiotic chromosome segregation pattern. Genes & development **27**:2147–2163. DOI: https://doi.org/10.1101/gad.224253.113

Borek WE, Vincenten N, Duro E, Makrantoni V, Spanos C, Sarangapani KK, de Lima Alves F, Kelly DA, Asbury CL, Rappsilber J, Marston AL. 2021. The Proteomic Landscape of Centromeric Chromatin Reveals an Essential Role for the Ctf19CCAN Complex in Meiotic Kinetochore Assembly. Current biology: CB **31**:283-296.e7. DOI: https://doi.org/10.1016/j.cub.2020.10.025, PMID: 33157029

Buonomo SBC, Rabitsch KP, Fuchs J, Gruber S, Sullivan M, Uhlmann F, Petronczki M, Tóth A, Nasmyth K. 2003. Division of the nucleolus and its release of CDC14 during anaphase of meiosis I depends on separase, SPO12, and SLK19. Developmental cell **4**:727–739.

Carlile TM, Amon A. 2008. Meiosis I is established through division-specific translational control of a cyclin. Cell **133**:280–291. DOI: https://doi.org/10.1016/j.cell.2008.02.032, PMID: 18423199

Chen C, Whitney IP, Banerjee A, Sacristan C, Sekhri P, Kern DM, Fontan A, Kops GJPL, Tyson JJ, Cheeseman IM, Joglekar AP. 2019. Ectopic Activation of the Spindle Assembly Checkpoint Signaling Cascade Reveals Its Biochemical Design. Current biology: CB **29**:104-119.e10. DOI: https://doi.org/10.1016/j.cub.2018.11.054, PMID: 30595520

Chen J, Liao A, Powers EN, Liao H, Kohlstaedt LA, Evans R, Holly RM, Kim JK, Jovanovic M, Ünal E. 2020. Aurora B-dependent Ndc80 degradation regulates kinetochore composition in meiosis. Genes & Development **34**:209–225. DOI: https://doi.org/10.1101/gad.333997.119

Chia M, van Werven FJ. 2016. Temporal Expression of a Master Regulator Drives Synchronous Sporulation in Budding Yeast. G3 (Bethesda, Md.) **6**:3553–3560. DOI: https://doi.org/10.1534/g3.116.034983

Clyne RK, Katis VL, Jessop L, Benjamin KR, Herskowitz I, Lichten M, Nasmyth K. 2003. Polo-like kinase Cdc5 promotes chiasmata formation and cosegregation of sister centromeres at meiosis I. Nat Cell Biol **5**:480–485.

Demichev V, Messner CB, Vernardis SI, Lilley KS, Ralser M. 2020. DIA-NN: neural networks and interference correction enable deep proteome coverage in high throughput. Nature Methods **17**:41–44. DOI: https://doi.org/10.1038/s41592-019-0638-x, PMID: 31768060

Duro E, Marston AL. 2015. From equator to pole: splitting chromosomes in mitosis and meiosis. Genes & Development **29**:109–122. DOI: https://doi.org/10.1101/gad.255554.114, PMID: 25593304

El Jailani S, Cladière D, Nikalayevich E, Touati SA, Chesnokova V, Melmed S, Buffin E, Wassmann K. 2025. Eliminating separase inhibition reveals absence of robust cohesin protection in oocyte metaphase II. The EMBO journal **44**:5187–5214. DOI: https://doi.org/10.1038/s44318-025-00522-0, PMID: 40764838

Fernius J, Marston AL. 2009. Establishment of cohesion at the pericentromere by the Ctf19 kinetochore subcomplex and the replication fork-associated factor, Csm3. PLoS genetics **5**:e1000629. DOI: https://doi.org/10.1371/journal.pgen.1000629, PMID: 19730685

Galander S, Barton RE, Borek WE, Spanos C, Kelly DA, Robertson D, Rappsilber J, Marston AL. 2019. Reductional Meiosis I Chromosome Segregation Is Established by Coordination of Key Meiotic Kinases. Developmental Cell **49**:526-541.e5. DOI: https://doi.org/10.1016/j.devcel.2019.04.003, PMID: 31031198

Ghodgaonkar-Steger M, Potocnjak M, Zimniak T, Fischböck-Halwachs J, Solis-Mezarino V, Singh S, Speljko T, Hagemann G, Drexler DJ, Witte G, Herzog F. 2020. C-Terminal Motifs of the MTW1 Complex Cooperatively Stabilize Outer Kinetochore Assembly in Budding Yeast. Cell Reports **32**:108190. DOI: https://doi.org/10.1016/j.celrep.2020.108190, PMID: 32997987

Gruhn JR, Hoffmann ER. 2022. Errors of the Egg: The Establishment and Progression of Human Aneuploidy Research in the Maternal Germline. Annual Review of Genetics **56**:369–390. DOI: https://doi.org/10.1146/annurev-genet-072820-033609, PMID: 36055648

Gui L, Homer H. 2012. Spindle assembly checkpoint signalling is uncoupled from chromosomal position in mouse oocytes. Development **139**:1941–1946. DOI: https://doi.org/10.1242/dev.078352

Havens KA, Gardner MK, Kamieniecki RJ, Dresser ME, Dawson DS. 2010. Slk19p of Saccharomyces cerevisiae regulates anaphase spindle dynamics through two independent mechanisms. Genetics **186**:1247–1260. DOI: https://doi.org/10.1534/genetics.110.123257, PMID: 20923975

Hayashi A, Asakawa H, Haraguchi T, Hiraoka Y. 2006. Reconstruction of the kinetochore during meiosis in fission yeast Schizosaccharomyces pombe. Molecular biology of the cell **17**:5173–5184. DOI: https://doi.org/10.1091/mbc.E06-05-0388

Heberle H, Meirelles GV, da Silva FR, Telles GP, Minghim R. 2015. InteractiVenn: a web-based tool for the analysis of sets through Venn diagrams. BMC bioinformatics **16**:169. DOI: https://doi.org/10.1186/s12859-015-0611-3, PMID: 25994840

Hochwagen A, Wrobel G, Cartron M, Demougin P, Niederhauser-Wiederkehr C, Boselli MG, Primig M, Amon A. 2005. Novel response to microtubule perturbation in meiosis. Mol Cell Biol **25**:4767–4781.

Holt LJ, Tuch BB, Villén J, Johnson AD, Gygi SP, Morgan DO. 2009. Global analysis of Cdk1 substrate phosphorylation sites provides insights into evolution. Science (New York, N.Y.) **325**:1682. DOI: https://doi.org/10.1126/science.1172867, PMID: 19779198

Iwabuchi M, Ohsumi K, Yamamoto TM, Sawada W, Kishimoto T. 2000. Residual Cdc2 activity remaining at meiosis I exit is essential for meiotic M-M transition in Xenopus oocyte extracts. The EMBO journal **19**:4513–4523. DOI: https://doi.org/10.1093/emboj/19.17.4513, PMID: 10970845

Katis VL, Galova M, Rabitsch KP, Gregan J, Nasmyth K. 2004. Maintenance of cohesin at centromeres after meiosis I in budding yeast requires a kinetochore-associated protein related to MEI-S332. Current biology : CB **14**:560–572.

Kim J, Ishiguro K-I, Nambu A, Akiyoshi B, Yokobayashi S, Kagami A, Ishiguro T, Pendás AM, Takeda N, Sakakibara Y, Kitajima TS, Tanno Y, Sakuno T, Watanabe Y. 2015. Meikin is a conserved regulator of meiosis-I-specific kinetochore function. Nature **517**:466–471.

Koch LB, Spanos C, Kelly V, Ly T, Marston AL. 2024. Rewiring of the phosphoproteome executes two meiotic divisions in budding yeast. The EMBO journal **43**:1351–1383. DOI: https://doi.org/10.1038/s44318-024-00059-8, PMID: 38413836

Kolano A, Brunet S, Silk AD, Cleveland DW, Verlhac M-H. 2012. Error-prone mammalian female meiosis from silencing the spindle assembly checkpoint without normal interkinetochore tension. Proceedings of the National Academy of Sciences **109**:E1858–E1867. DOI: https://doi.org/10.1073/pnas.1204686109

Kolberg L, Raudvere U, Kuzmin I, Vilo J, Peterson H. 2020. gprofiler2 -- an R package for gene list functional enrichment analysis and namespace conversion toolset g:Profiler. F1000Research **9**:ELIXIR-709. DOI: https://doi.org/10.12688/f1000research.24956.2, PMID: 33564394

Kouznetsova A, Kitajima TS, Brismar H, Höög C. 2019. Post-metaphase correction of aberrant kinetochore-microtubule attachments in mammalian eggs. EMBO Reports **20**:e47905. DOI: https://doi.org/10.15252/embr.201947905, PMID: 31290587

Lane SIR, Yun Y, Jones KT. 2012. Timing of anaphase-promoting complex activation in mouse oocytes is predicted by microtubule-kinetochore attachment but not by bivalent alignment or tension. Development **139**:1947–1955. DOI: https://doi.org/10.1242/dev.077040

Lee BH, Amon A. 2003. Role of Polo-like kinase CDC5 in programming meiosis I chromosome segregation. Science (New York, N.Y.) **300**:482–486.

Leontiou I, London N, May KM, Ma Y, Grzesiak L, Medina-Pritchard B, Amin P, Jeyaprakash AA, Biggins S, Hardwick KG. 2019. The Bub1-TPR Domain Interacts Directly with Mad3 to Generate Robust Spindle Checkpoint Arrest. Current biology: CB **29**:2407-2414.e7. DOI: https://doi.org/10.1016/j.cub.2019.06.011, PMID: 31257143

Liang F-S, Ho WQ, Crabtree GR. 2011. Engineering the ABA plant stress pathway for regulation of induced proximity. Science Signaling **4**:rs2. DOI: https://doi.org/10.1126/scisignal.2001449, PMID: 21406691

Liu D, Vleugel M, Backer CB, Hori T, Fukagawa T, Cheeseman IM, Lampson MA. 2010. Regulated targeting of protein phosphatase 1 to the outer kinetochore by KNL1 opposes Aurora B kinase. The Journal of Cell Biology **188**:809–820. DOI: https://doi.org/10.1083/jcb.201001006, PMID: 20231380

Lo HC, Wan L, Rosebrock A, Futcher B, Hollingsworth NM. 2008. Cdc7-Dbf4 regulates NDT80 transcription as well as reductional segregation during budding yeast meiosis. Molecular biology of the cell **19**:4956–4967.

MacKenzie A, Vicory V, Lacefield S. 2023. Meiotic cells escape prolonged spindle checkpoint activity through kinetochore silencing and slippage. PLOS Genetics **19**:e1010707. DOI: https://doi.org/10.1371/journal.pgen.1010707, PMID: 37018287

Marston AL, Lee BH, Amon A. 2003. The Cdc14 phosphatase and the FEAR network control meiotic spindle disassembly and chromosome segregation. Developmental Cell **4**:711–726. DOI: https://doi.org/10.1016/s1534-5807(03)00130-8, PMID: 12737806

Marston ALL, Tham W-HH, Shah H, Amon A. 2004. A genome-wide screen identifies genes required for centromeric cohesion. Science (New York, N.Y.) **303**:1367–1370. DOI: https://doi.org/10.1126/science.1094220

Maskell DP, Hu X-W, Singleton MR. 2010. Molecular architecture and assembly of the yeast kinetochore MIND complex. The Journal of Cell Biology **190**:823–834. DOI: https://doi.org/10.1083/jcb.201002059, PMID: 20819936

Matos J, Lipp JJ, Bogdanova A, Guillot S, Okaz E, Junqueira M, Shevchenko A, Zachariae W. 2008. Dbf4-dependent CDC7 kinase links DNA replication to the segregation of homologous chromosomes in meiosis I. Cell **135**:662–678.

McAinsh AD, Kops GJPL. 2023. Principles and dynamics of spindle assembly checkpoint signalling. Nature Reviews Molecular Cell Biology **24**:543–559. DOI: https://doi.org/10.1038/s41580-023-00593-z

Mehta GD, Agarwal M, Ghosh SK. 2014. Functional characterization of kinetochore protein, Ctf19 in meiosis I: An implication of differential impact of Ctf19 on the assembly of

mitotic and meiotic kinetochores in Saccharomyces cerevisiae. Molecular Microbiology **91**:1179–1199. DOI: https://doi.org/10.1111/mmi.12527

Mengoli V, Jonak K, Lyzak O, Lamb M, Lister LM, Lodge C, Rojas J, Zagoriy I, Herbert M, Zachariae W. 2021. Deprotection of centromeric cohesin at meiosis II requires APC/C activity but not kinetochore tension. The EMBO Journal **40**:e106812. DOI: https://doi.org/10.15252/embj.2020106812, PMID: 33644894

Meyer RE, Chuong HH, Hild M, Hansen CL, Kinter M, Dawson DS. 2015. Ipl1/Aurora-B is necessary for kinetochore restructuring in meiosis I in Saccharomyces cerevisiae. Molecular biology of the cell **26**:2986–3000. DOI: https://doi.org/10.1091/mbc.E15-01-0032

Miller MP, Ünal E, Brar GA, Amon A. 2012. Meiosis I chromosome segregation is established through regulation of microtubule–kinetochore interactions. eLife **1**:e00117. DOI: https://doi.org/10.7554/eLife.00117

Miyazono K-I, Miyakawa T, Sawano Y, Kubota K, Kang H-J, Asano A, Miyauchi Y, Takahashi M, Zhi Y, Fujita Y, Yoshida T, Kodaira K-S, Yamaguchi-Shinozaki K, Tanokura M. 2009. Structural basis of abscisic acid signalling. Nature **462**:609–614. DOI: https://doi.org/10.1038/nature08583, PMID: 19855379

Nagaoka SI, Hodges CA, Albertini DF, Hunt PA. 2011. Oocyte-Specific Differences in Cell-Cycle Control Create an Innate Susceptibility to Meiotic Errors. Current Biology **21**:651–657. DOI: https://doi.org/10.1016/j.cub.2011.03.003

Palframan WJ, Meehl JB, Jaspersen SL, Winey M, Murray AW. 2006. Anaphase inactivation of the spindle checkpoint. Science (New York, N.Y.) **313**:680–684.

Peshkin L, Daldello EM, Itallie EV, Sonnett M, Kreuzer J, Haas W, Kirschner MW, Jessus C. 2025. Decoding protein phosphorylation during oocyte meiotic divisions using phosphoproteomics. eLife **13**. DOI: https://doi.org/10.7554/eLife.104255.2

Peters J-M. 2006. The anaphase promoting complex/cyclosome: a machine designed to destroy. Nature Reviews Molecular Cell Biology **7**:644–656. DOI: https://doi.org/10.1038/nrm1988

Petronczki M, Matos J, Mori S, Gregan J, Bogdanova A, Schwickart M, Mechtler K, Shirahige K, Zachariae W, Nasmyth K. 2006. Monopolar attachment of sister kinetochores at meiosis I requires casein kinase 1. Cell **126**:1049–1064.

Petrovic A, Mosalaganti S, Keller J, Mattiuzzo M, Overlack K, Krenn V, De Antoni A, Wohlgemuth S, Cecatiello V, Pasqualato S, Raunser S, Musacchio A. 2014. Modular assembly of RWD domains on the Mis12 complex underlies outer kinetochore organization. Molecular Cell **53**:591–605. DOI: https://doi.org/10.1016/j.molcel.2014.01.019, PMID: 24530301

Pinsky BA, Kung C, Shokat KM, Biggins S. 2006. The Ipl1-Aurora protein kinase activates the spindle checkpoint by creating unattached kinetochores. Nature Cell Biology **8**:78–83. DOI: https://doi.org/10.1038/ncb1341, PMID: 16327780

Plowman R, Singh N, Tromer EC, Payan A, Duro E, Spanos C, Rappsilber J, Snel B, Kops GJPL, Corbett KD, Marston AL. 2019. The molecular basis of monopolin recruitment to the kinetochore. Chromosoma **128**:331–354. DOI: https://doi.org/10.1007/s00412-019-00700-0, PMID: 31037469

Ptacek J, Devgan G, Michaud G, Zhu H, Zhu X, Fasolo J, Guo H, Jona G, Breitkreutz A, Sopko R, McCartney RR, Schmidt MC, Rachidi N, Lee S-J, Mah AS, Meng L, Stark MJR, Stern DF, De Virgilio C, Tyers M, Andrews B, Gerstein M, Schweitzer B, Predki PF, Snyder M. 2005. Global analysis of protein phosphorylation in yeast. Nature **438**:679–684. DOI: https://doi.org/10.1038/nature04187

Rappsilber J, Mann M, Ishihama Y. 2007. Protocol for micro-purification, enrichment, pre-fractionation and storage of peptides for proteomics using StageTips. Nature Protocols **2**:1896–1906. DOI: https://doi.org/10.1038/nprot.2007.261, PMID: 17703201

Rosenberg JS, Cross FR, Funabiki H. 2011. KNL1/Spc105 Recruits PP1 to Silence the Spindle Assembly Checkpoint. Current biology : CB **21**:942–947. DOI: https://doi.org/10.1016/j.cub.2011.04.011, PMID: 21640906

Roy B, Sim J, Han SJY, Joglekar AP. 2022. Kre28-Spc105 interaction is essential for Spc105 loading at the kinetochore. Open Biology **12**:210274. DOI: https://doi.org/10.1098/rsob.210274, PMID: 35042402

Roy B, Verma V, Sim J, Fontan A, Joglekar AP. 2019. Delineating the contribution of Spc105-bound PP1 to spindle checkpoint silencing and kinetochore microtubule attachment regulation. The Journal of Cell Biology **218**:3926–3942. DOI: https://doi.org/10.1083/jcb.201810172, PMID: 31649151

Salah SM, Nasmyth K. 2000. Destruction of the securin Pds1p occurs at the onset of anaphase during both meiotic divisions in yeast. Chromosoma **109**:27–34.

Sarangapani KK, Akiyoshi B, Duggan NM, Biggins S, Asbury CL. 2013. Phosphoregulation promotes release of kinetochores from dynamic microtubules via multiple mechanisms. Proceedings of the National Academy of Sciences of the United States of America **110**:7282–7287. DOI: https://doi.org/10.1073/pnas.1220700110, PMID: 23589891

Sarangapani KK, Duro E, Deng Y, Alves F de L, Ye Q, Opoku KN, Ceto S, Rappsilber J, Corbett KD, Biggins S, Marston AL, Asbury CL. 2014. Sister kinetochores are mechanically fused during meiosis I in yeast. Science (New York, N.Y.) **346**:248–251. DOI: https://doi.org/10.1126/science.1256729, PMID: 25213378

Sarkar S, Shenoy RT, Dalgaard JZ, Newnham L, Hoffmann E, Millar JBA, Arumugam P. 2013. Monopolin subunit Csm1 associates with MIND complex to establish monopolar attachment of sister kinetochores at meiosis I. PLoS genetics **9**:e1003610. DOI: https://doi.org/10.1371/journal.pgen.1003610, PMID: 23861669

Sebestova J, Danylevska A, Novakova L, Kubelka M, Anger M. 2012. Lack of response to unaligned chromosomes in mammalian female gametes. Cell Cycle (Georgetown, Tex.) **11**:3011–3018. DOI: https://doi.org/10.4161/cc.21398, PMID: 22871737

Stegmeier F, Visintin R, Amon A. 2002. Separase, polo kinase, the kinetochore protein Slk19, and Spo12 function in a network that controls Cdc14 localization during early anaphase. Cell **108**:207–220.

Sullivan M, Lehane C, Uhlmann F. 2001. Orchestrating anaphase and mitotic exit: separase cleavage and localization of Slk19. Nat Cell Biol **3**:771–777.

Tanaka K, Chang HL, Kagami A, Watanabe Y. 2009. CENP-C functions as a scaffold for effectors with essential kinetochore functions in mitosis and meiosis. Developmental cell **17**:334–343.

Wagih O. 2017. ggseqlogo: a versatile R package for drawing sequence logos. Bioinformatics (Oxford, England) **33**:3645–3647. DOI: https://doi.org/10.1093/bioinformatics/btx469, PMID: 29036507

Wettstein R, Hugener J, Gillet L, Hernández-Armenta Y, Henggeler A, Xu J, van Gerwen J, Wollweber F, Arter M, Aebersold R, Beltrao P, Pilhofer M, Matos J. 2024. Waves of regulated protein expression and phosphorylation rewire the proteome to drive gametogenesis in budding yeast. Developmental Cell **59**:1764-1782.e8. DOI: https://doi.org/10.1016/j.devcel.2024.05.025, PMID: 38906138

Wiśniewski JR, Zougman A, Nagaraj N, Mann M. 2009. Universal sample preparation method for proteome analysis. Nature Methods **6**:359–362. DOI: https://doi.org/10.1038/nmeth.1322

Zhang X, Smits AH, van Tilburg GB, Ovaa H, Huber W, Vermeulen M. 2018. Proteome-wide identification of ubiquitin interactions using UbIA-MS. Nature Protocols **13**:530–550. DOI: https://doi.org/10.1038/nprot.2017.147, PMID: 29446774

1312 **Supplementary Table 1** List of plasmids used in this study
1313
1314 **Supplementary Table 2** List of strains used in this study
1315
1316 **Source Code 1** R script used for mass spectrometry analysis and figure generation in this
1317 study.
1318

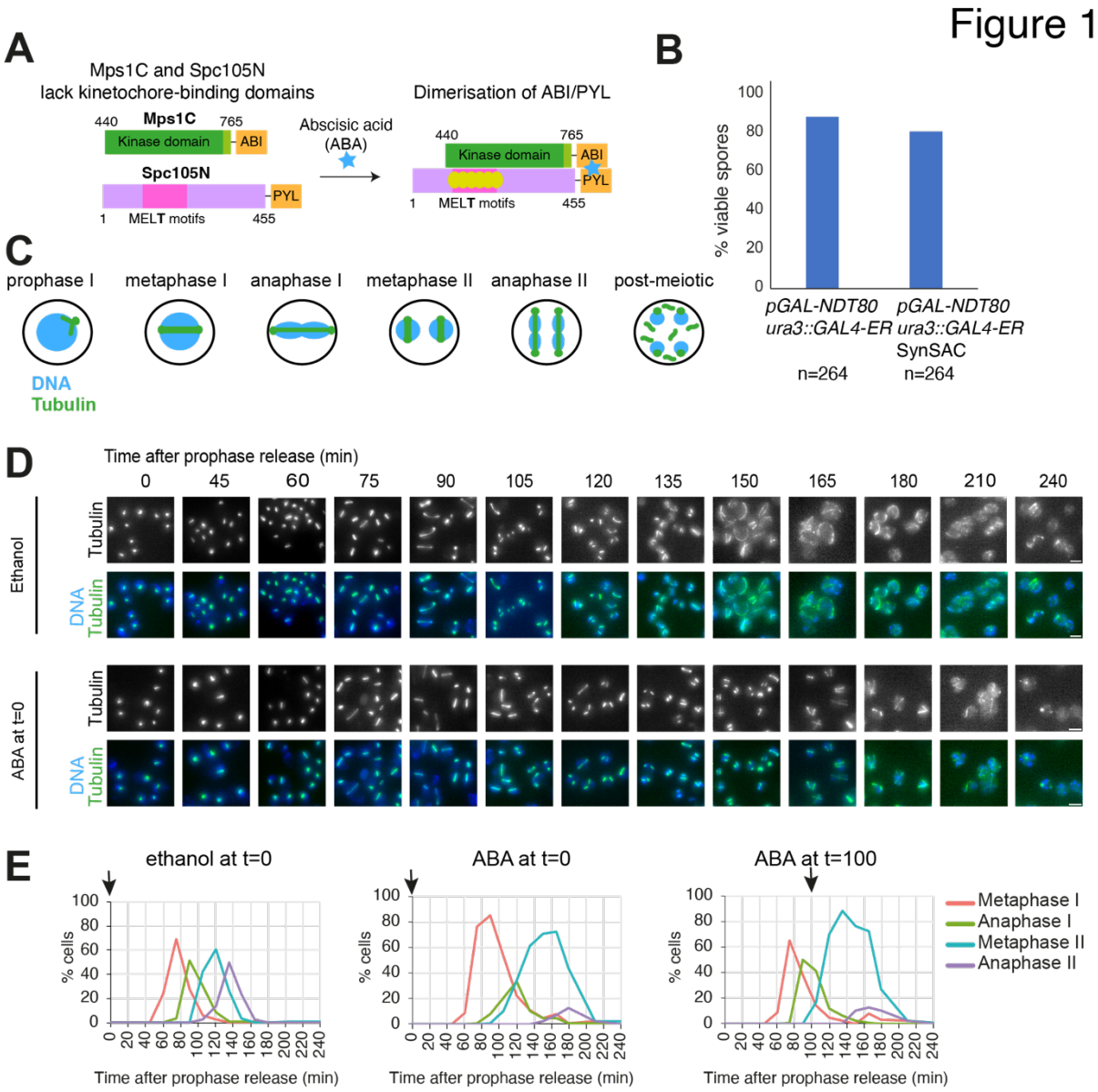

Figure 1 The meiotic SynSAC activation system

(A) Schematic of synthetic SAC dimerization system. (B) Spore viability of wild type (AM11189) and SynSAC dimer (AM30783) yeast strains (C) Schematic showing spindle morphology at different stages in meiosis. (D and E) SynSAC strain AM30783 was released from prophase by β-oestradiol addition under control (ethanol, left), meiosis I dimerizing (250μM ABA at release), or meiosis II dimerizing (250μM ABA at 100 minutes) conditions. (D) Representative images of fields of SynSAC cells at the indicated times after prophase release. Upper panels (ethanol) show control cells where SynSAC is not activated, lower panels (ABA) show cells where SynSAC is activated from prophase release. Scale bar = 5μm. (E) Scoring of spindle morphology after anti-tubulin immunofluorescence. 100 cells were scored at each timepoint. Arrow indicates time of ethanol or ABA addition.

1332

1333

Figure 2

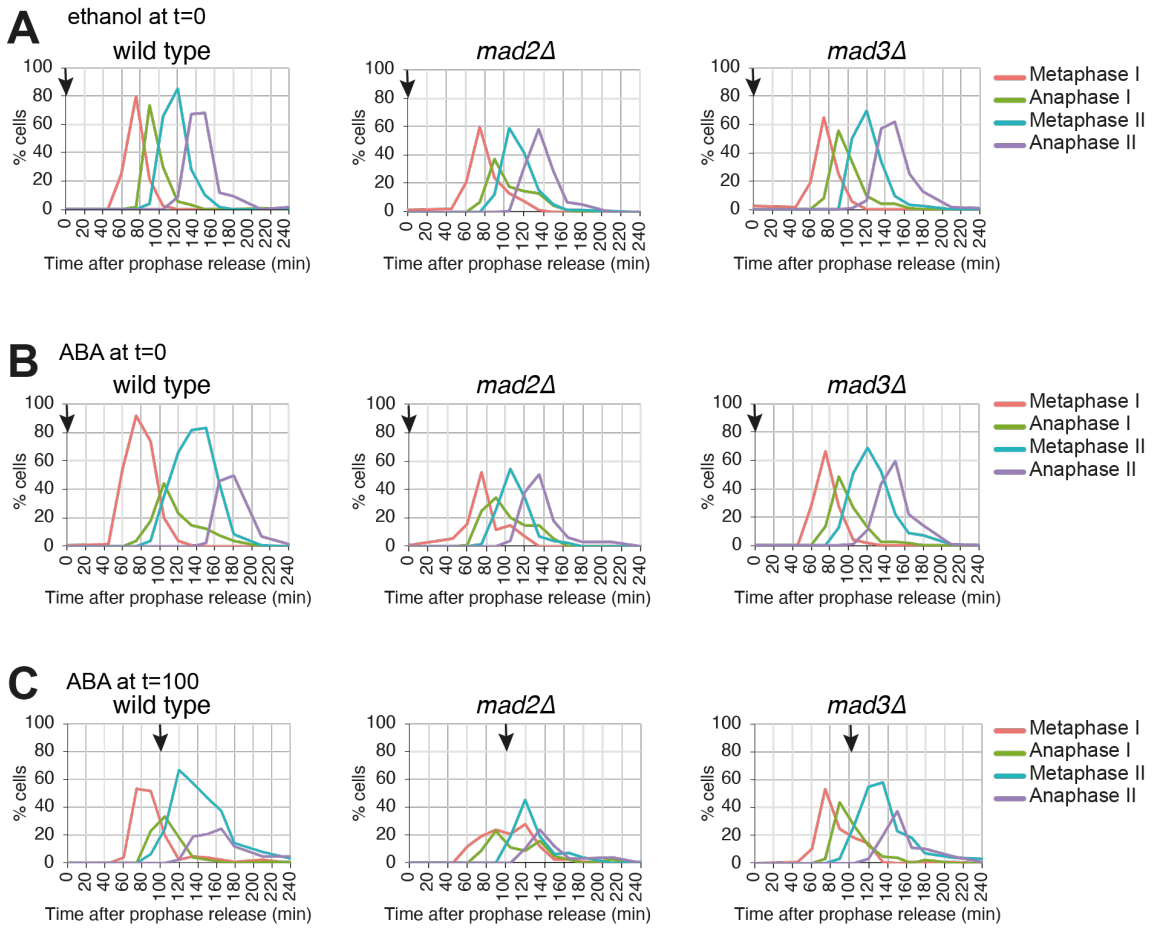

1334
1335
1336
1337
1338 **Figure 2 SynSAC activation depends on checkpoint proteins**
1339 (A-C) Meiosis spindle immunofluorescence timecourse in wild-type SynSAC (AM30783),
1340 SynSAC SynSAC *mad2Δ* (AM33559), and SynSAC *mad3Δ* (AM30784) strains. All strains
1341 were released from prophase by β-oestradiol addition. (A) Control cells where ethanol was
1342 added at release (B) SynSAC dimerisation was induced by addition 250μM abscisic acid at
1343 prophase release (C) SynSAC dimerisation was induced by addition 250μM of abscisic acid
1344 100 minutes after release. 100 cells were scored at each timepoint.
1345
1346

Figure 2-figure supplement 1

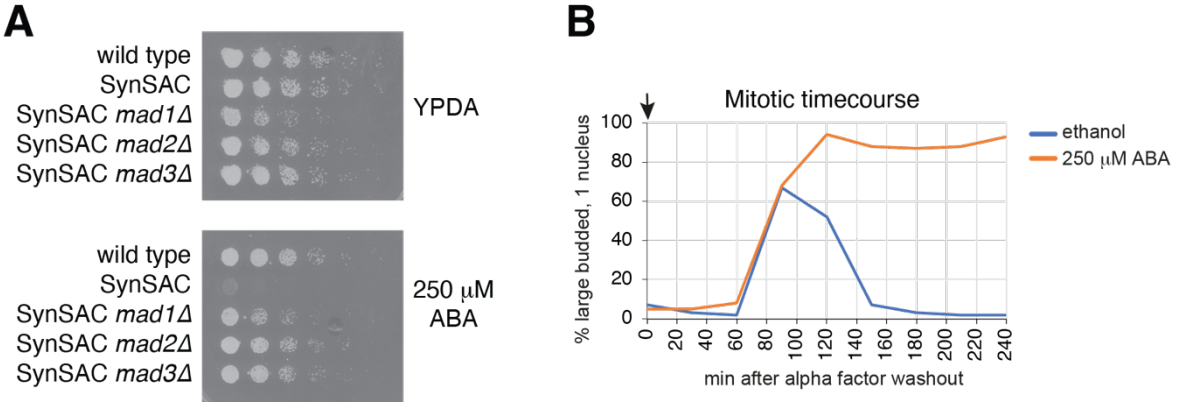

Figure 2- figure supplement 1. SynSAC induces a robust ABA-induced mitotic arrest (A) Serial dilution mitotic growth assay of wild-type (AM11189), SynSAC (AM30783), SynSAC *mad1Δ* (AM33558), SynSAC *mad2Δ* (AM33559), and SynSAC *mad3Δ* (AM30784) strains on YPDA rich media (top) and YPDA with 250μM ABA (bottom). (B) Mitotic SynSAC arrest timecourse. Yeast cultures of wild-type haploid SynSAC strain AM30663 were arrested in G1 with alpha factor and released into fresh media. Cultures were treated with either control solvent (ethanol) or ABA to induce SynSAC dimerization. The fraction of cells with large buds and one nucleus after DAPI-staining was determined after scoring 100 cells for each timepoint.

Figure 3

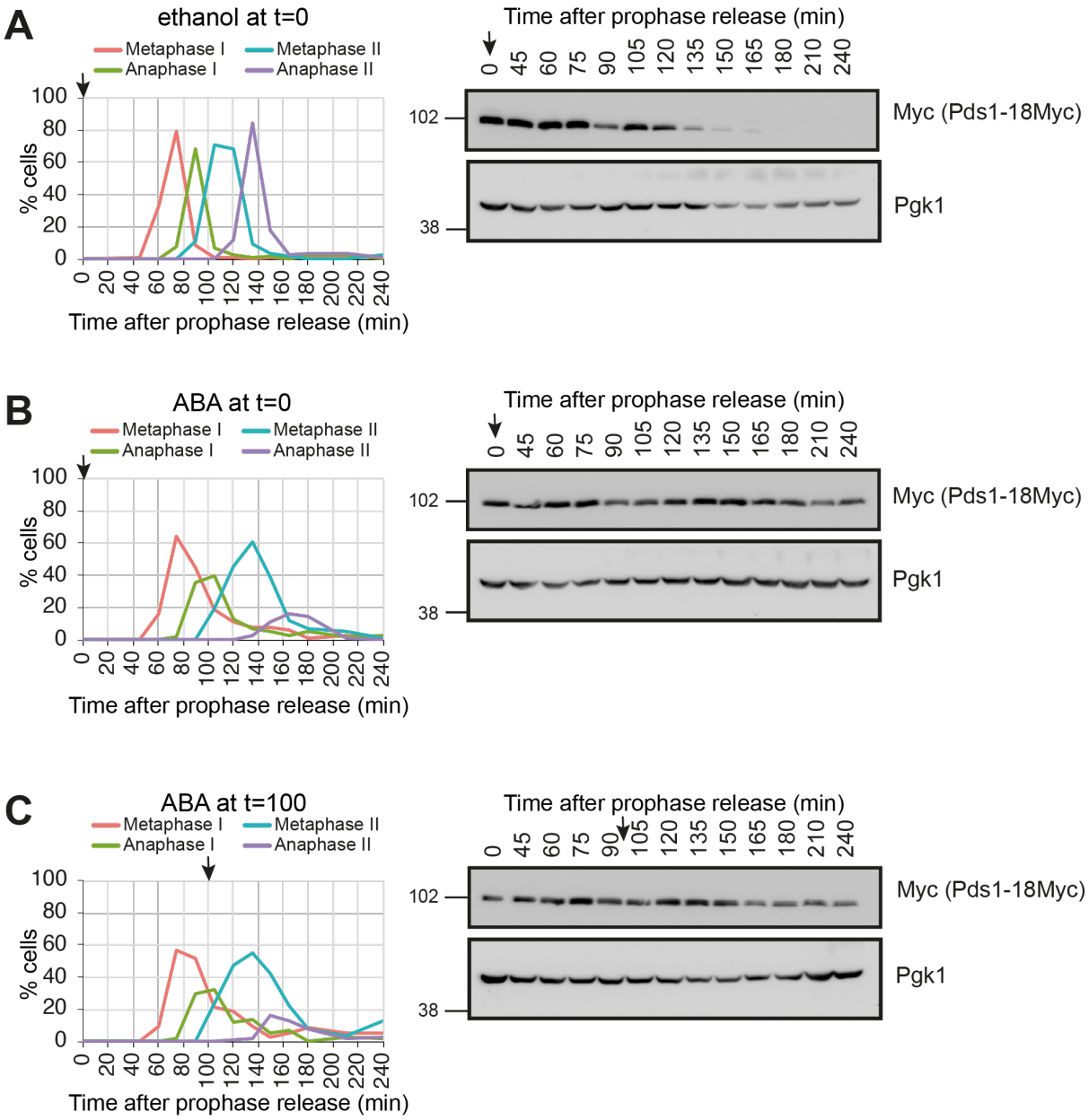

Figure 3 Meiotic SynSAC delays degradation of Pds1^{securin}

(A-C) Meiosis timecourse with spindle immunofluorescence (left) and western blotting to visualize Pds1-Myc and Pgk1 loading control (right). (A) Control timecourse with ethanol added at prophase release. (B) Meiosis I SynSAC delay timecourse with 250μM ABA added at prophase release. (C) Meiosis II SynSAC delay meiosis timecourse with 250μm ABA added at 100 minutes after prophase release (vertical dotted line). Strain used in A-C was AM34398. For the spindle counts, 100 cells were scored at each timepoint. Arrows indicate the time of ethanol or ABA addition.

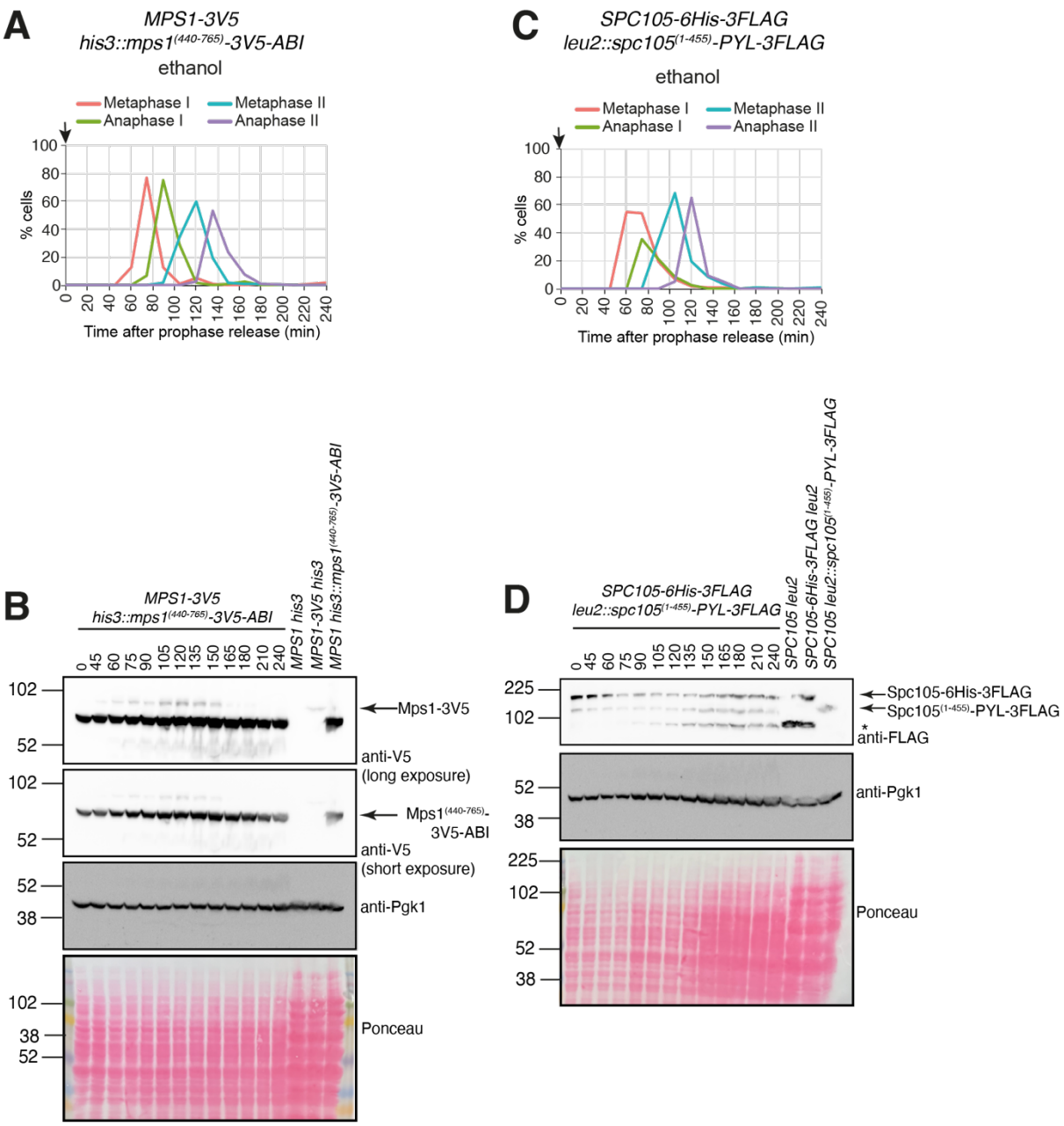

Figure 3-figure supplement 1. Protein levels of the SynSAC dimer constructs do not significantly change throughout meiosis.

(A and B) Meiotic timecourse after release from prophase of a strain expressing V5-tagged full-length endogenous Mps1 in addition to the Mps1$^{(440-765)}$-ABI-3V5 SynSAC dimer construct (AM34816). (A) Spindle morphology after scoring 100 cells per timepoint. Arrows indicate time of ethanol addition. (B) Western blot analysis of samples at the indicated timepoints. Extracts from cycling wild-type (AM1828), *MPS1-3V5* (34733) and his3::Mps1$^{(440-765)}$-3V5-ABI (33850) strains were run as controls. (C and D) Meiotic timecourse of a strain expressing Flag-tagged

1379 full-length endogenous Spc105 in addition to the Spc105$^{(1-455)}$-PYL-3Flag SynSAC dimer
1380 construct (AM34817). (C) Spindle morphology at the indicated timepoints were scored after
1381 tubulin immunofluorescence. (D) Western blot analysis of samples harvested at the indicated
1382 timepoints. Extracts from cycling wild-type (AM1828), Spc105-6His-3Flag (AM34876) and
1383 leu2::Spc105$^{(1-455)}$-PYL-3Flag (AM30735) strains run as controls. * indicates a background
1384 band present in the untagged control strain.
1385

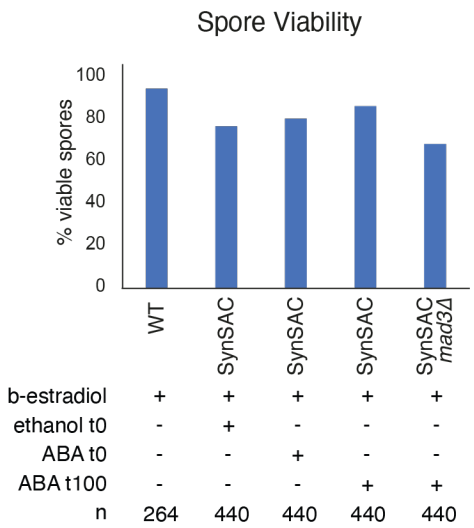

Figure 3-figure supplement 2. SynSAC does not affect spore viability after meiosis

Spore viability assay of SynSAC strains following meiosis I or meiosis II SynSAC activation. Following meiotic timecourses with the indicated treatments, tetrads were collected and dissected on rich media plates. The number of spores which grew colonies was counted. Strains analysed were wild type (AM11189), SynSAC (AM30783) and SynSAC *mad3Δ* (30784).

Figure 4

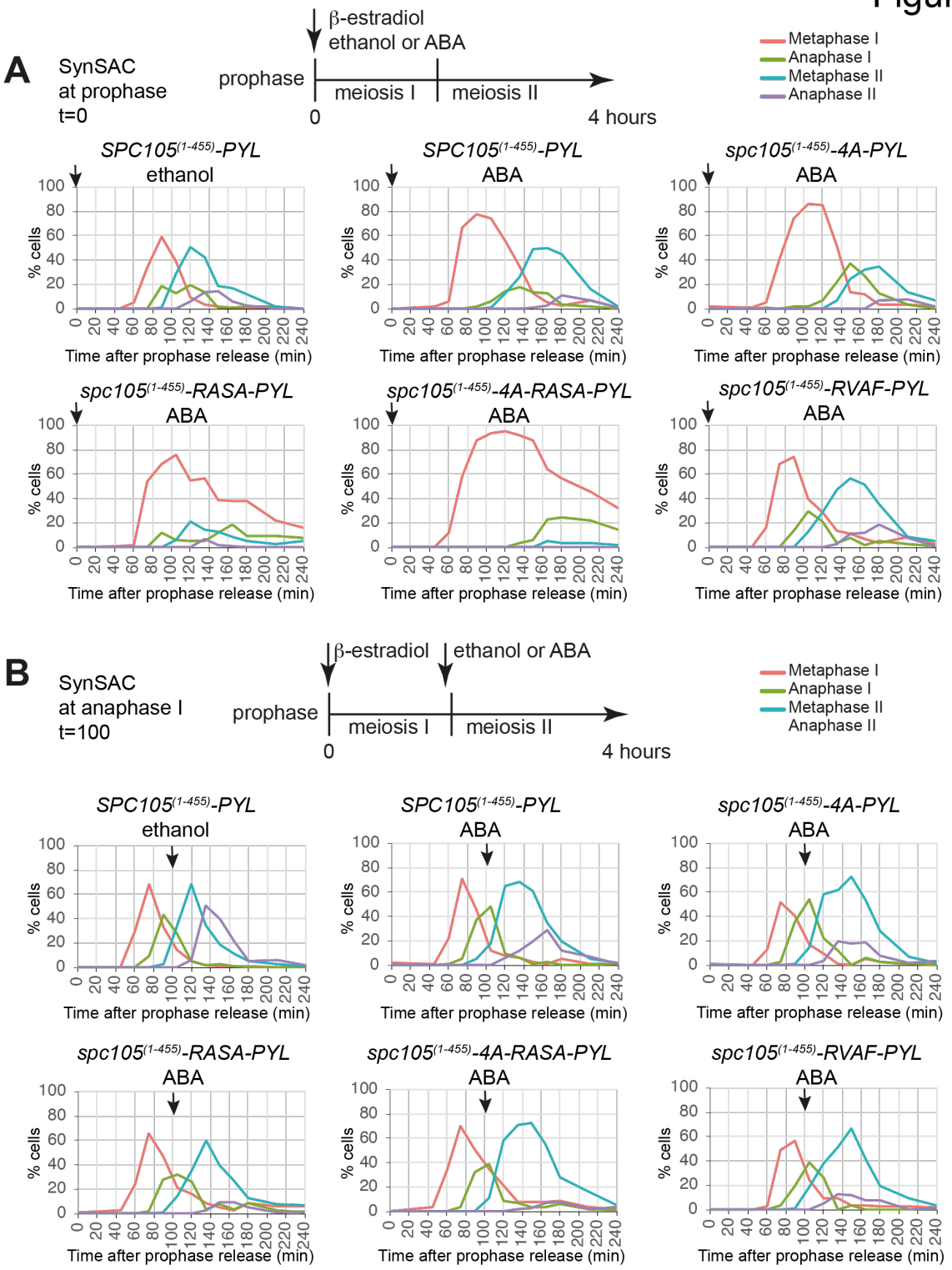

Figure 4 PP1 binding restrains SynSAC delay duration in meiotic metaphase

(A and B) Meiosis I (A) and meiosis II (B) SynSAC spindle immunofluorescence timecourses in wild-type vs PP1 binding site mutant SynSAC strains. Top: Schematic indicating drug addition timing. Middle row: Control wild-type (AM30783), SynSAC wild-type (AM30783), SynSAC *spc105-4A* (AM34201). Bottom row: SynSAC *spc105-RASA* (AM34203), SynSAC

1402 *spc105-4A-RASA* (AM34202), SynSAC *spc105-RVAF* (AM34487). Arrows indicate the time
1403 of ethanol/ABA addition. 100 cells were scored at each timepoint.
1404

Figure 4-figure supplement 1

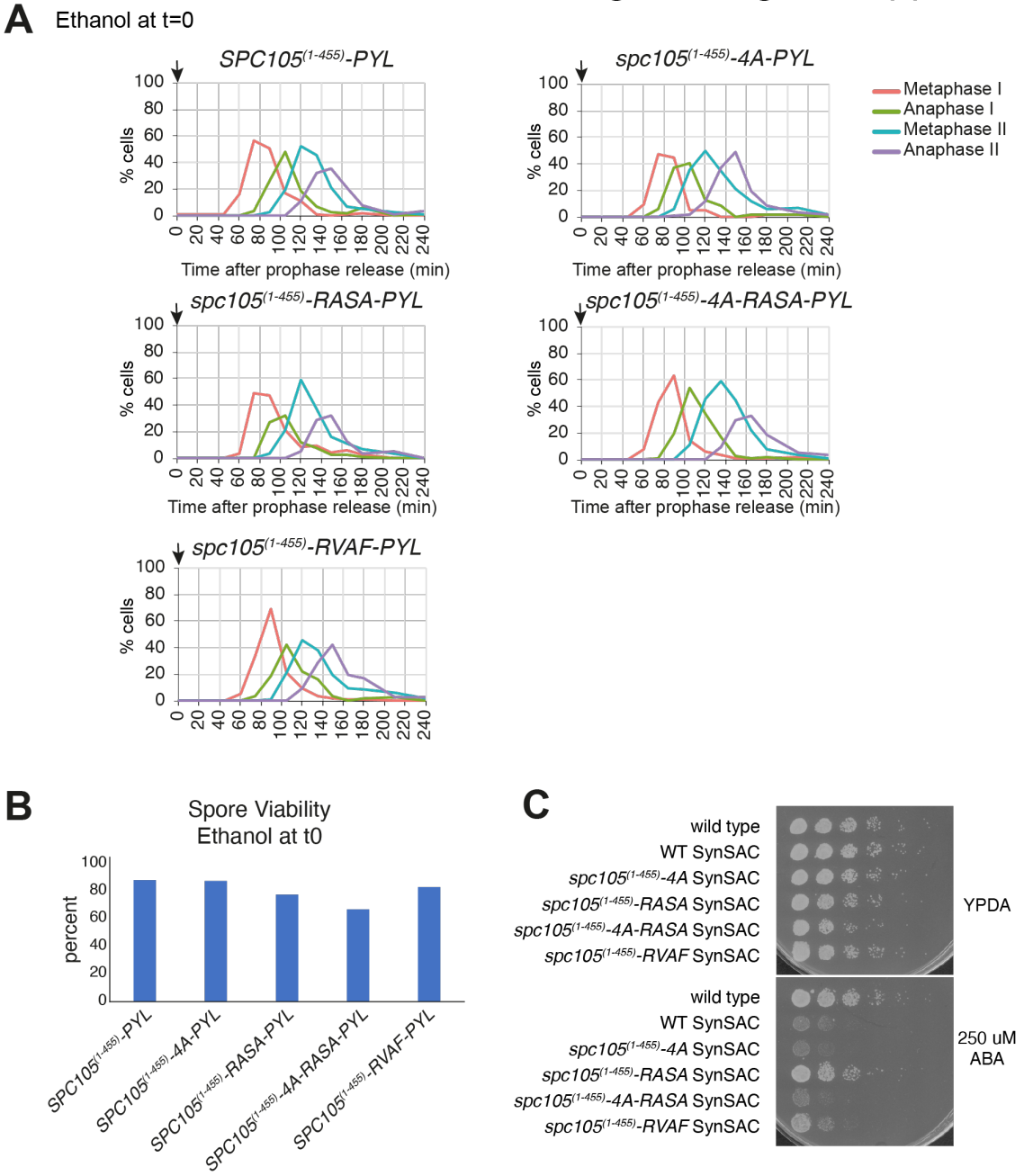

Figure 4-figure supplement 1. Mutation of the PP1 binding sites in the Spc105 SynSAC construct does not affect timing of meiosis, spore viability, or mitotic growth. (A) Meiotic spindle immunofluorescence timecourses of control treated wild-type *SPC105*$^{(1-455)}$*-PYL* (AM30783), *spc105*$^{(1-455)}$*-4A-PYL* (AM34201), *spc105*$^{(1-455)}$*-RASA-PYL* (AM34203), *spc105*$^{(1-455)}$*-4A-RASA-PYL* (AM34202), and *spc105*$^{(1-455)}$*-RVAF-PYL* (AM34487) strains. Arrows indicates time of ethanol addition. 100 cells were scored for each timepoint. (B) Spore viability of wild-type and PP1 binding site mutant SynSAC strains. Tetrads from control treated meiotic timecourses as in (A) (ethanol added at prophase release), were collected and dissected on rich media. The number of colonies which grew from dissected

1415 spores was counted. (C) Serial dilution mitotic growth assay of wild-type and PP1 binding
1416 site mutant SynSAC strains as in (A) on YPDA and YPDA with 250μM ABA media.
1417

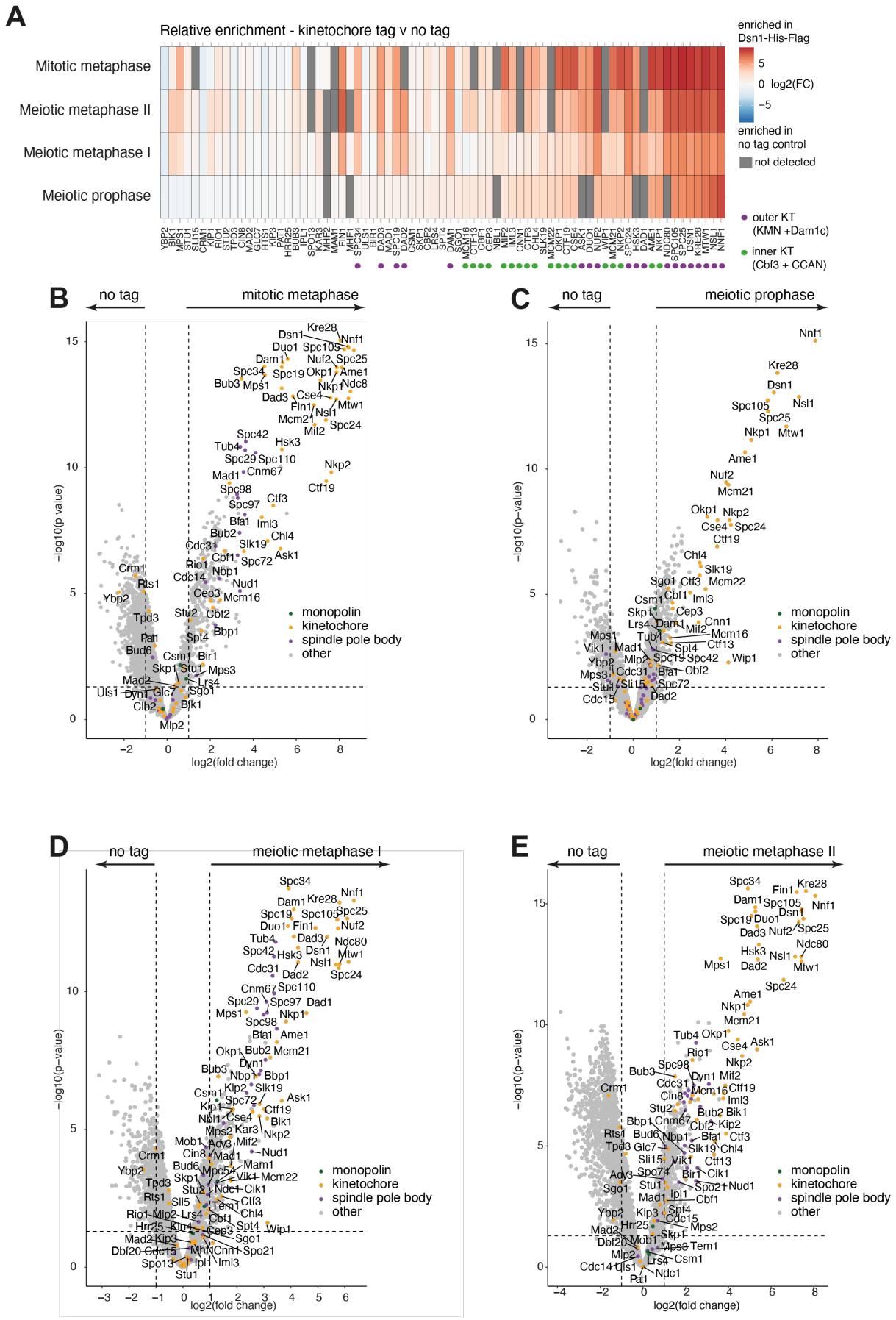
A
Relative enrichment - kinetochore tag v no tag
Mitotic metaphase
Meiotic metaphase II
Meiotic metaphase I
Meiotic prophase
enriched in Dsn1-His-Flag
5
0 log2(FC)
−5
enriched in no tag control
not detected
outer KT (KMN +Dam1c)
inner KT (Cbf3 + CCAN)
B
no tag
mitotic metaphase
−log10(p value)
log2(fold change)
monopolin
kinetochore
spindle pole body
other
C
no tag
meiotic prophase
−log10(p−value)
log2(fold change)
monopolin
kinetochore
spindle pole body
other
D
no tag
meiotic metaphase I
−log10(p−value)
log2(fold change)
monopolin
kinetochore
spindle pole body
other
E
no tag
meiotic metaphase II
−log10(p−value)
log2(fold change)
monopolin
kinetochore
spindle pole body
other

1418

1419 **Figure 5 Kinetochore composition in mitotic metaphase, meiotic prophase, meiotic**
1420 **metaphase I and meiotic metaphase II.** (A) Heatmap showing the fold change enrichment
1421 level of each kinetochore protein at each stage, for the tag vs no tag comparison. (B-D)
1422 Volcano plots comparing unscaled protein levels of Dsn-6His-3FLAG (tag) to no tag after
1423 anti-FLAG immunoprecipitation from matched extracts of mitotic metaphase (B), meiotic
1424 prophase (C), metaphase I (D) and metaphase II (E). Strains used are no tag (AM30990) or
1425 *DSN1-6His-3Flag* (AM33675).
1426
1427

Figure 5-figure supplement 1

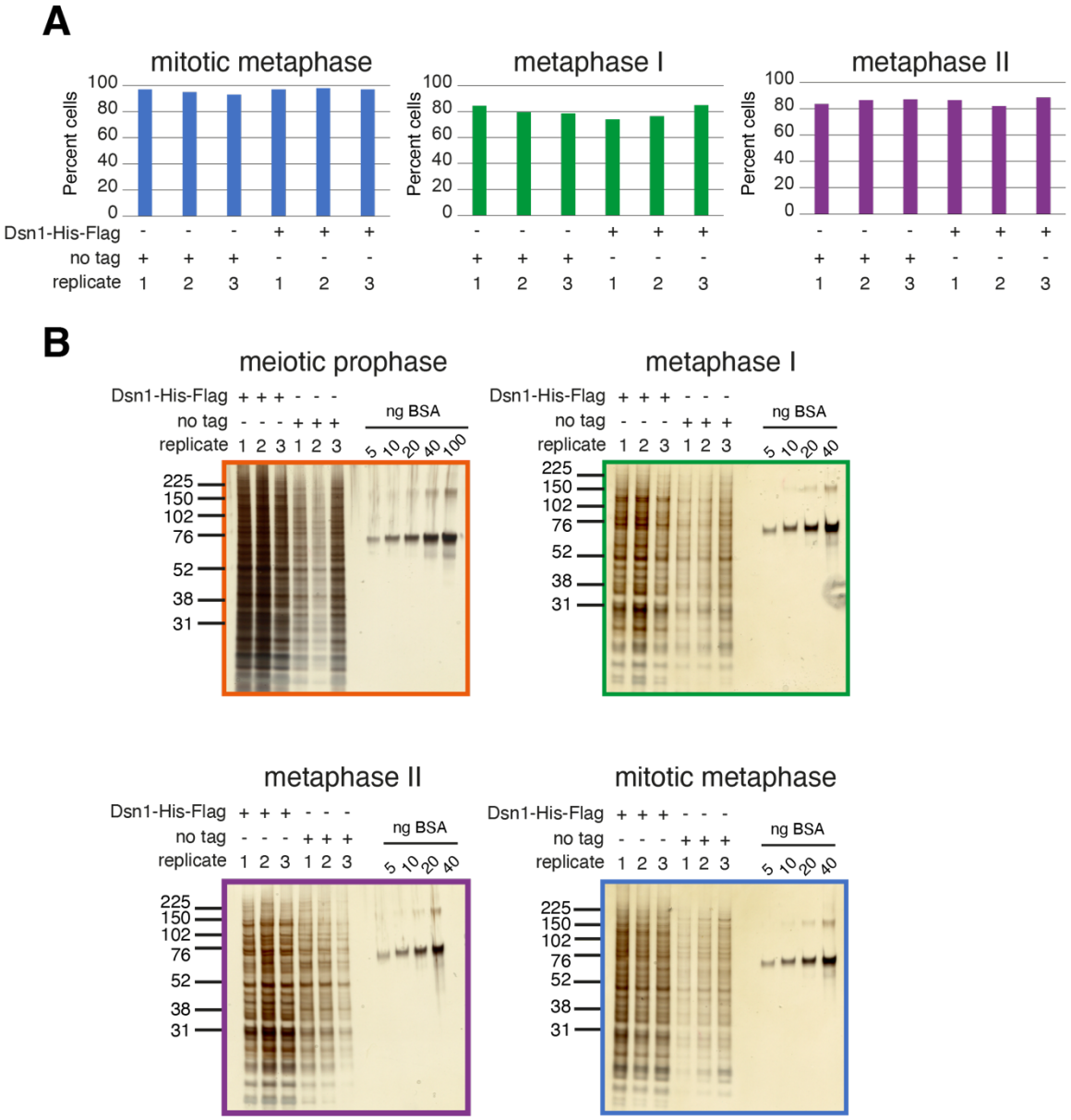

Figure 5-figure supplement 1. Immunoprecipitation of kinetochores from meiotic prophase, metaphase I, metaphase II and mitotic metaphase

(A and B) Kinetochores were purified from the indicated cell cycle stages by anti-FLAG immunoprecipitation of Dsn1-6His-3FLAG (AM33675) and compared to no tag (strain AM30990). (A) Enrichment of cells at the indicated metaphase stages was confirmed by scoring spindle morphology after tubulin immunofluorescence. (B) Silver-stained gels of control no-tag and Dsn1-6His-3Flag immunoprecipitations are shown.

Figure 5-figure supplement 2

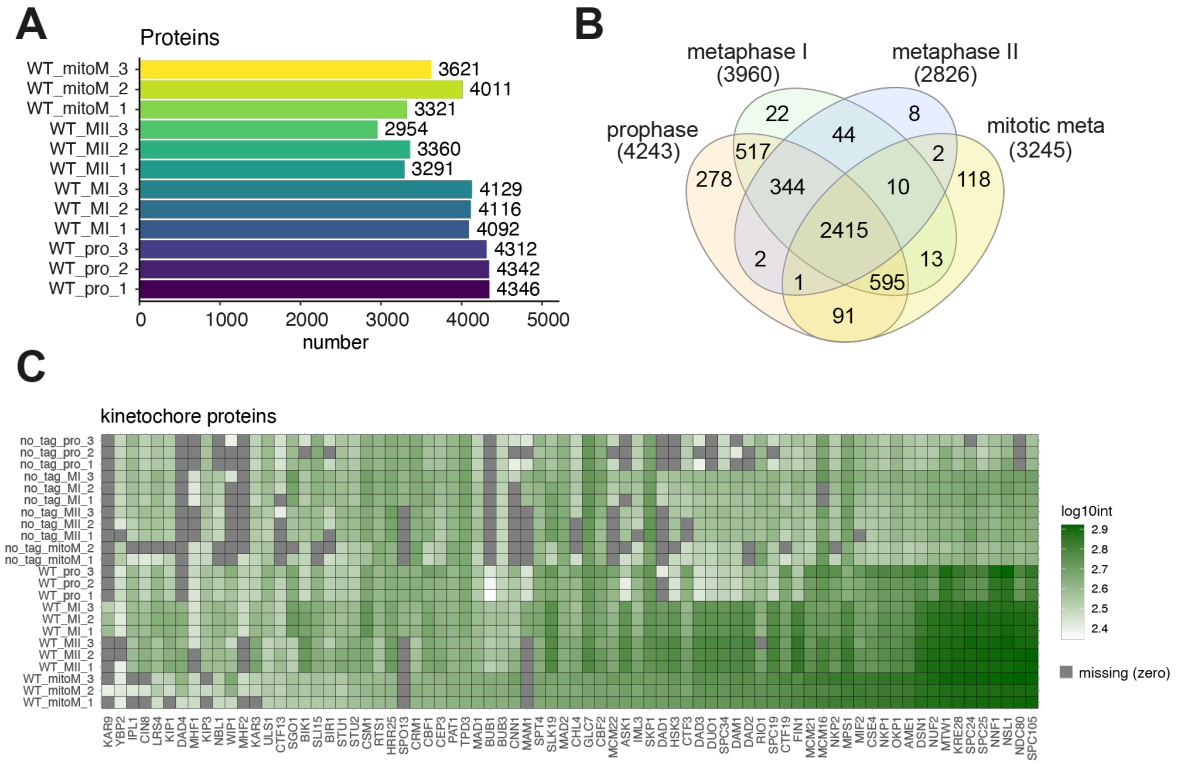

Figure 5-figure supplement 2. Kinetochore composition in meiosis

(A and B) Analysis of kinetochore composition after Dsn1 immunoprecipitation at different cell cycle stages. (A) Barplot of number of proteins detected in each *DSN1-6His-3Flag* IP sample from the indicated stage and replicate. (B) Venn diagram showing the number of proteins detected in each *DSN1-6His-3FLAG* IP sample and the overlap of which proteins were unique to each sample or shared between samples. Proteins were counted as included in a group if they were detected in all replicates of that sample type. (C) Kinetochore protein enrichment in kinetochore and control immunoprecipitations. Heatmap showing the abundance of each kinetochore protein in all immunoprecipitation samples analysed. Grey indicates missing values.

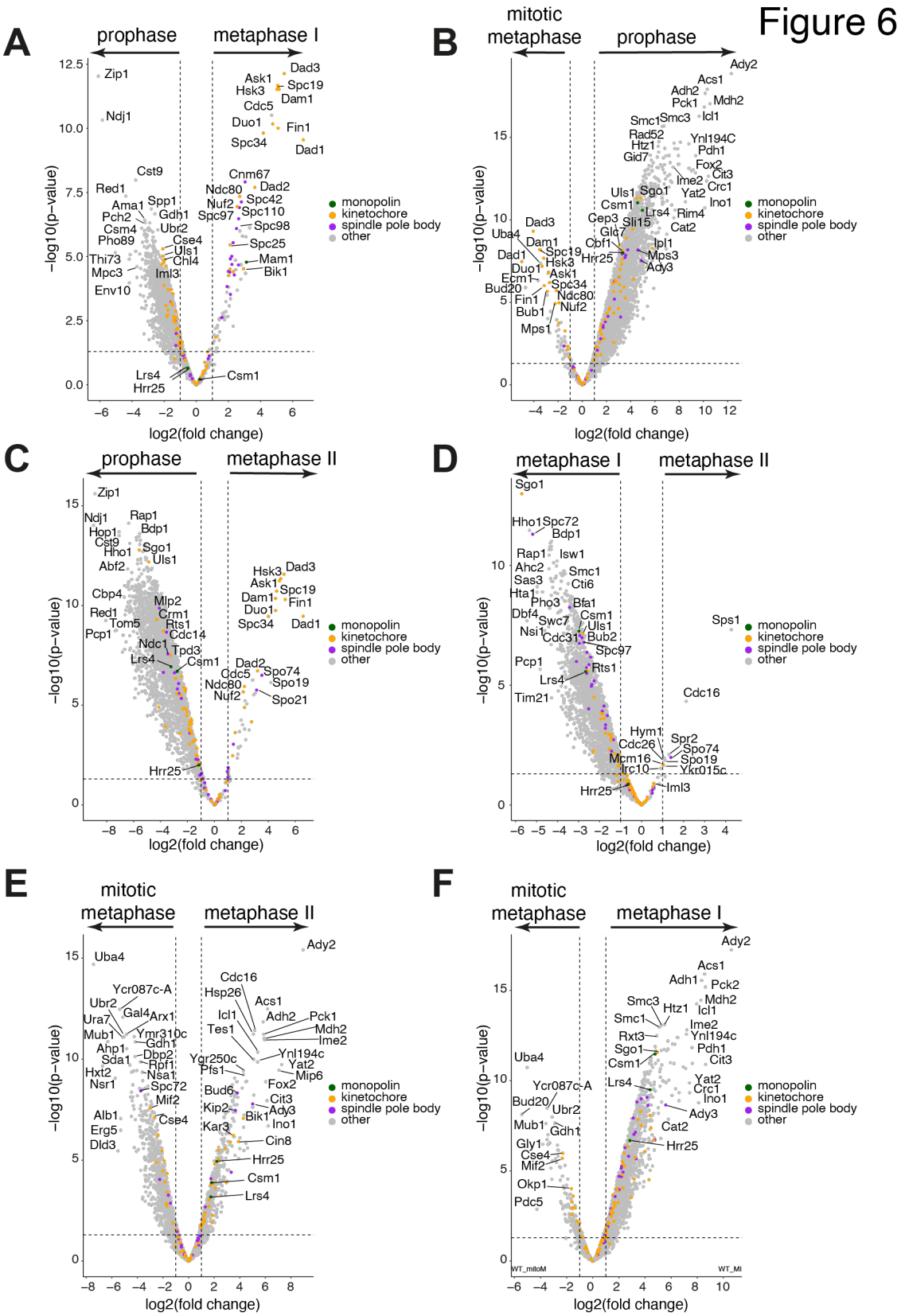

1449

1450

1451 **Figure 6. Volcano plots of differential protein enrichment for each pair-wise**

1452 **comparison between different cell cycle stages**

1453 Comparisons of protein abundance detected by mass spectrometry in kinetochore
1454 purifications at the different stages. (A) Volcano plot comparing Dsn1-scaled protein levels in
1455 meiotic prophase (left) vs metaphase I (right). (B) Volcano plot comparing Dsn1-scaled
1456 protein levels in mitotic metaphase (left) vs meiotic prophase (right). (C) Volcano plot
1457 comparing Dsn1-scaled protein levels in meiotic prophase (left) vs metaphase II (right). (D)
1458 Volcano plot comparing Dsn1-scaled protein levels in metaphase I (left) vs metaphase II
1459 (right). (E) Volcano plot comparing Dsn1-scaled protein levels in mitotic metaphase (left) vs
1460 metaphase II (right). (F) Volcano plot comparing Dsn1-scaled protein levels in mitotic
1461 metaphase (left) vs metaphase I (right).
1462

Figure 6-figure supplement 1

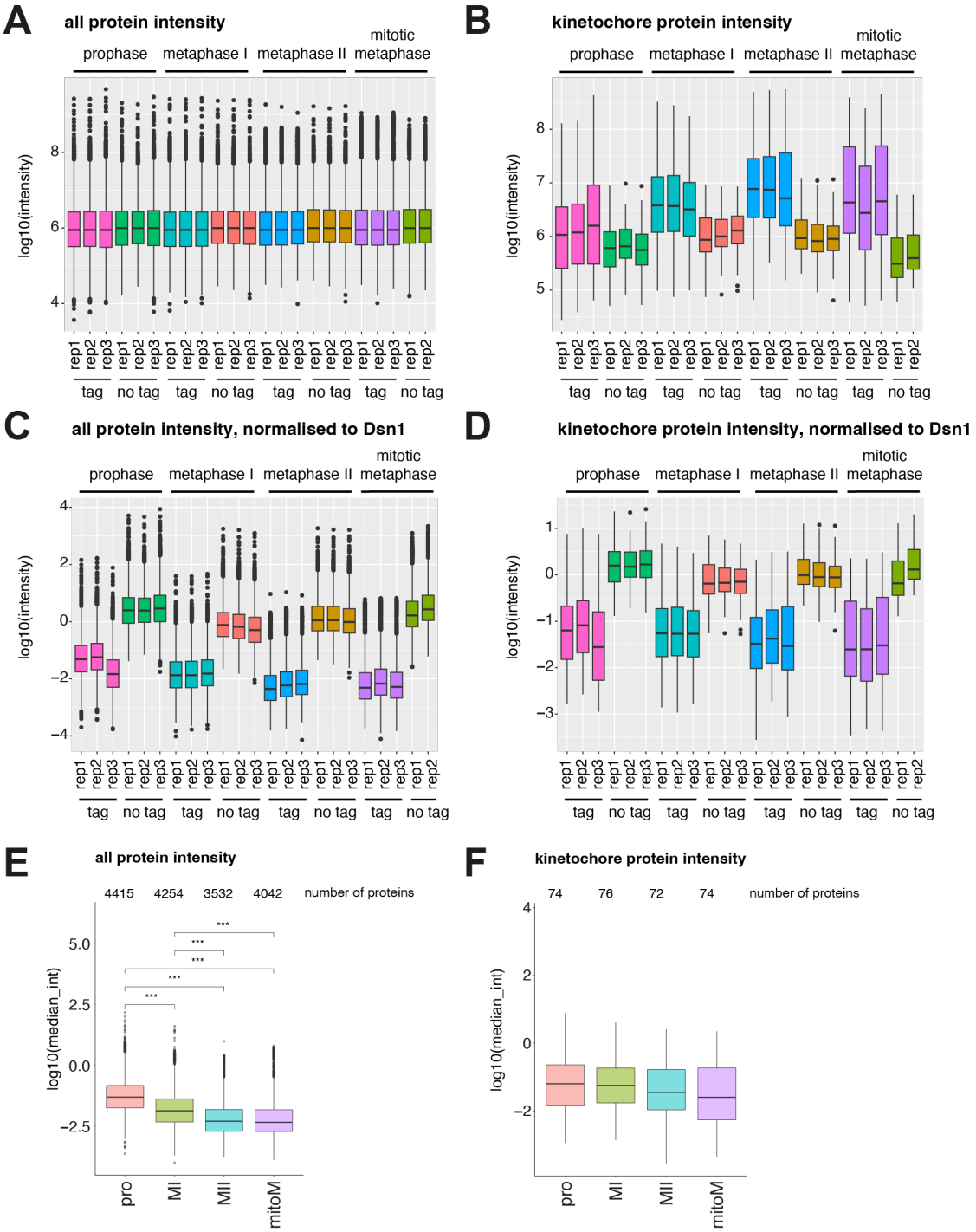

Figure 6-figure supplement 1. Total protein and kinetochore protein abundances before and after scaling to Dsn1

(A-F) Mass spectrometry analysis of Flag immunoprecipitations from no tag (AM30990) or *DSN1-6His-3Flag* (AM33675) strains. (A) Protein abundances (intensities) of all IP samples analysed by MS. (B) Kinetochore protein abundances of all IP samples analysed by MS. (C) Protein abundances after scaling to the Dsn1 protein level in each sample. (D) Kinetochore

1471 protein abundances after scaling to the Dsn1 protein level in each sample. (E) Protein
1472 abundances of the 4 *DSN1-6His-3Flag* sample types. Proteins were included if they were
1473 detected in all replicates of that stage. (F) Kinetochore protein abundances of the 4 *DSN1-*
1474 *His-3Flag* sample types. Proteins were included if they were detected in all replicates of that
1475 stage.
1476

A

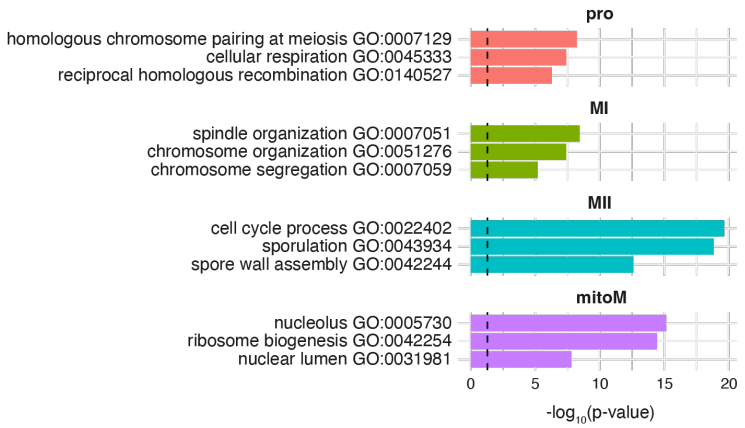

B

Enrichment ↑

pro vs MI	pro vs MII	pro vs mitoM	MI vs MII	MI vs mitoM	MI vs pro	MII vs MI	MII vs mitoM	MII vs pro	mitoM vs MI	mitoM vs MII	mitoM vs pro
ZIP1	NDJ1	ADY2	DBF4	ADY2	CDC5	SPS1	ADY2	SPO19	BUD20	UBA4	BUD20
NDJ1	ZIP1	MDH2	HHO1	CIT3	TEP1	CDC16	YAT2	SPO74	UBA4	HXT2	ECM1
THI73	RED1	CIT3	SPC72	PCK1	PES4	SPO74	MIP6	SPO21	PDC5	MUB1	UBA4
RED1	PCP1	ACS1	HTA1	ACS1	SPO19	SPR2	INO1	PES4	GLY1	NSR1	ALB1
MPC3	TOM5	CRC1	SAS3	ADH2	CNM67	SPO19	ACS1	SSP1	MUB1	DLD3	NSR1
ENV10	HOP1	ADH2	PCP1	MDH2	CLB4	SPS22	CIT3	CDC5	NAF1	YCR087C-A	YCR087C-A
PHO89	CST9	INO1	ABF2	INO1	SPC42	CDC26	FOX2	RRT5	YCR087C-A	ERG5	PXR1
CST9	TIM21	PCK1	NSI1	ICL1	CLB1	HYM1	IME2	CDC16	HXT2	ALB1	NAF1
EMC10	CSM4	ICL1	SWC7	FOX2	RRT5	YKR015C	MDH2	SPS22	ALB1	GAL4	YCR100C
COX12	CBP4	PDH1	AHC2	PDH1	SPO23	ASE1	PCK1	HYM1	DBP3	URA7	REI1
TOM5	FSF1	FOX2	RAP1	CRC1	SPC110	IRC10	ADH2	TEP1	TPO1	UBR2	RNH203
MHT1	ADR1	SFC1	IOC2	YAT2	SPC98	CDA1	ICL1	DON1	NSR1	ARX1	TMA23
COX7	COX4	CIT2	PHO3	IME2	SPO21	SMA1	YNL194C	CDC26	UBR2	AHP1	NHP2
OLE1	COX6	MLS1	IOC4	YNL194C	SPR1	CDH1	CDC16	CLB1	PXR1	SDA1	GLY1
ATP14	SCO2	YNL194C	HHT1	CIT2	SPC97	CHS5	PDH1	PFS1	GDH1	DBP3	DBP3
CSM4	COX12	YAT2	SKO1	MLS1	SSP1	MPC54	TES1	MRK1	REI1	THI7	FIR1
NCE103	POR1	ATO3	CBP4	RIM4	DON1	YHL012W	HSP26	MIP6	FSH1	PHO3	EBP2
COX4	COX5A	NUS1	BRF1	MIP6	NUD1	CIK1	CIT2	SUT1	DBP2	YEF3	NOP15
ATP19	ABF2	GUT2	HTZ1	AMS1	YLR146W-A	SPO21	ADY3	CDA1	ARX1	ERG11	ESF1
FTR1	DFM1	ACH1	MOT3	ATO3	SPC29	BCH1	CRC1	CNM67	RSA4	RRP36	DBP2

Figure 6-figure supplement 2. Identity and function of proteins enriched on kinetochores at distinct stages

(A) GO term enrichment of the selected terms among the top 50 non-kinetochore proteins co-purified at each stage. (B) Top 20 non-kinetochore proteins, ranked by increasing fold change enrichment in the first stage listed vs the second stage. (For example prophase vs MI, proteins are ranked by enrichment in prophase.)

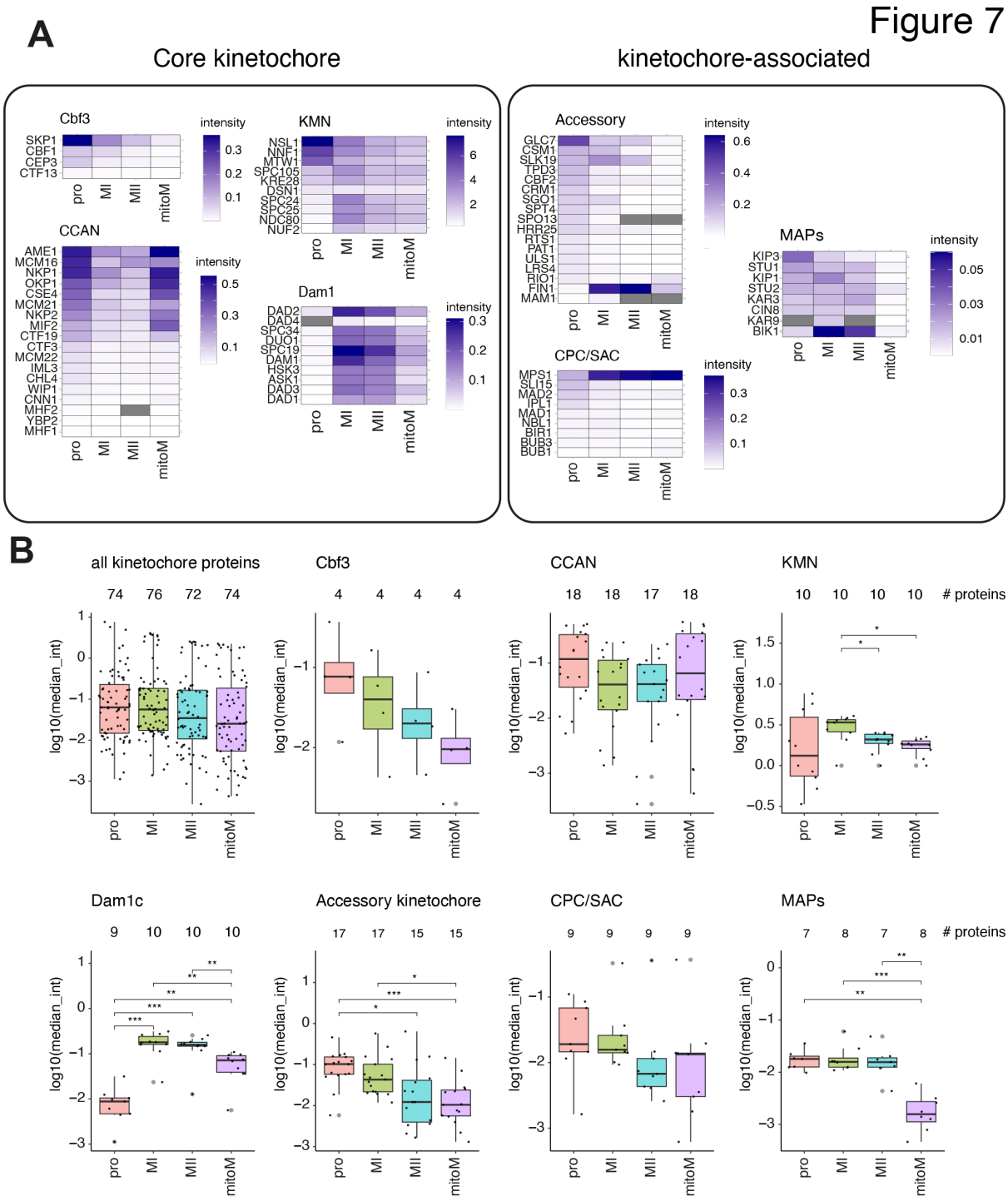

Figure 7 Kinetochore protein dynamics in meiotic prophase, metaphase I, metaphase II, and mitotic metaphase

(A and B) Kinetochores purified by Dsn1-6His-3Flag immunoprecipitation were analysed from cells arrested at the indicated stages using the SynSAC system by mass spectrometry. Strain used was AM33675. Protein levels are Dsn1-scaled. (A) Heatmap of individual protein levels of core kinetochore proteins (left). Heatmap of individual protein levels of kinetochore-associated proteins at each stage (right). (B) Boxplots of groups of kinetochore proteins at each stage. Dots indicate individual proteins and the numbers above each plot indicate the

1494 number of proteins included in each group at that stage. P-values from Wilcoxon two-sided
1495 test are shown.
1496

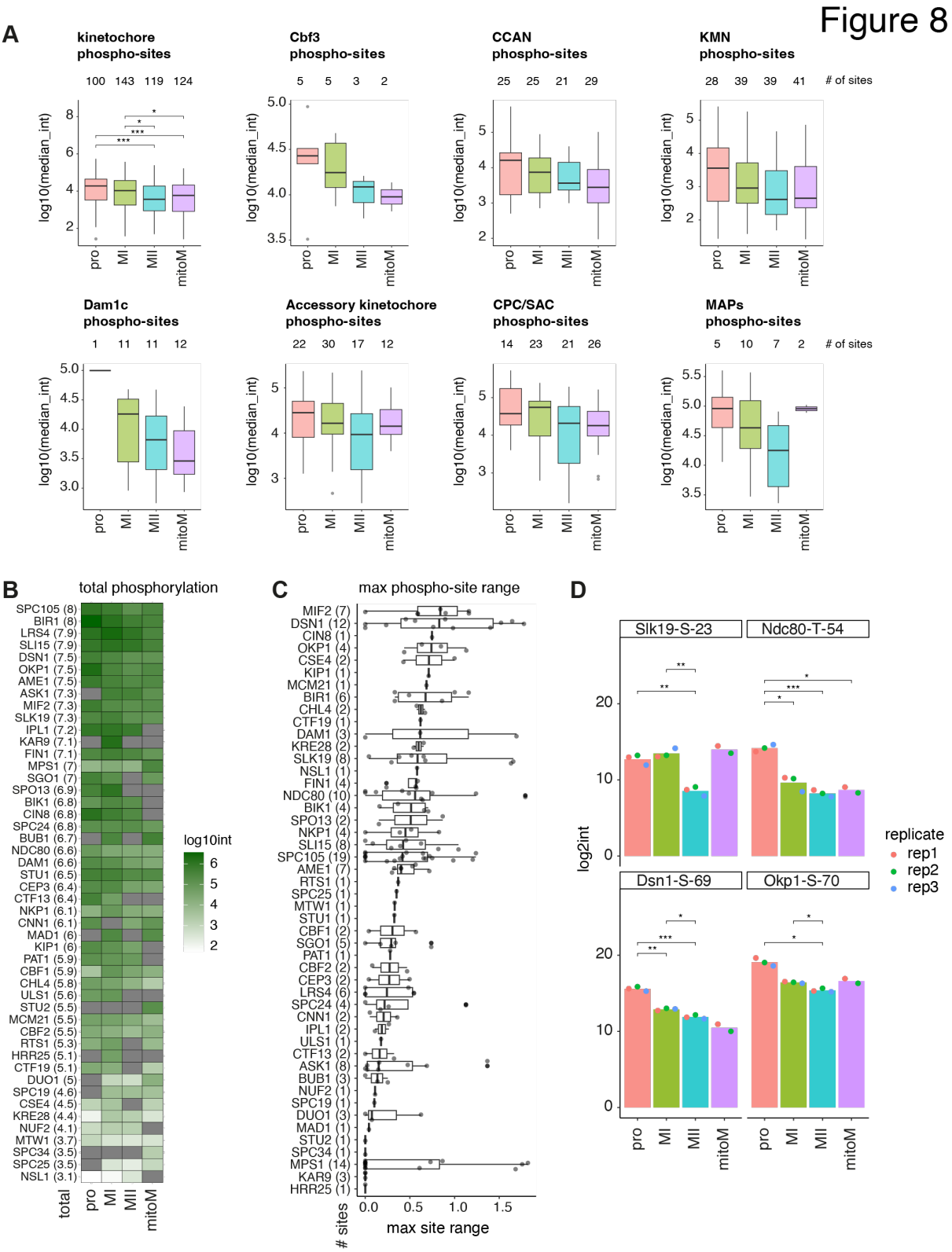

Figure 8 Reduced kinetochore protein phosphorylation in metaphase II

(A-D) Phosphorylation analysis of kinetochores purified as in Figure 5 and subjected to phospho-enrichment prior to mass spectrometry. (A) Boxplots of groups of kinetochore protein phosphorylation sites at each stage. Numbers above each plot indicate the number of phospho-sites included in the group at each stage. P-values from two-sided Wilcoxon test are

1503 shown for all kinetochore phospho-sites (upper left). No other comparisons were significantly
1504 different by Wilcoxon test in any other group/stage. (B) Heatmap of total sum of phospho-site
1505 abundance for each kinetochore protein at each stage. Phospho-proteins are ranked, with
1506 proteins with the highest sum of phospho-site abundances, for all 4 stages together, at the
1507 top. Numbers within parentheses next to protein name indicate the sum of phospho-site
1508 abundances for all 4 stages. (C) Boxplots of maximum phospho-site range across the 4 stages
1509 for each kinetochore protein. Phospho-proteins are ranked so that proteins with the highest
1510 median phospho-site dynamic range across stages are at the top. Numbers in parentheses
1511 indicate the number of phospho-sites considered to calculate maximum phospho-site range.
1512 (D) Barplots of individual phospho-site abundances for the indicated sites at each of the 4
1513 stages. Dots indicate the abundance in individual replicates. P-values from two-sided t-test
1514 are indicated.
1515

Figure 8-figure supplement 1

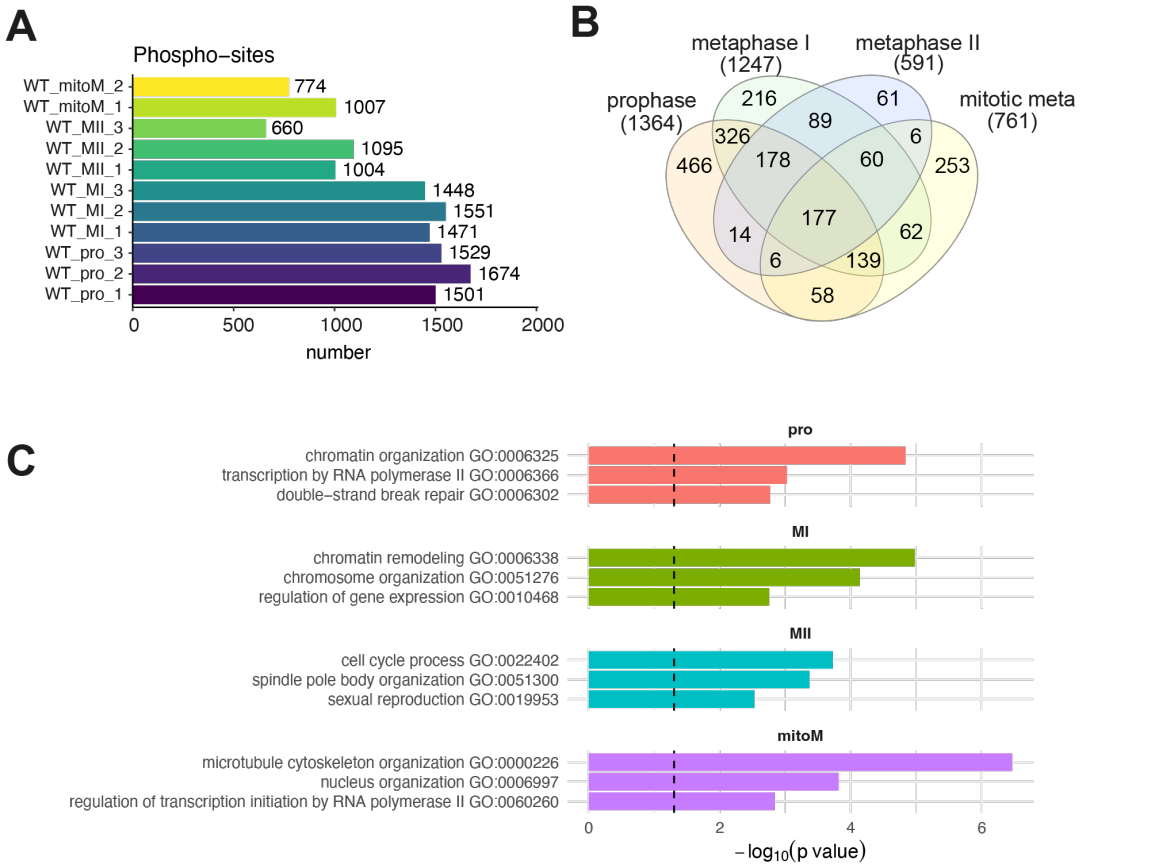

D

Enrichment ↑

pro_v_MI	pro_v_MII	pro_v_mitoM	MI_v_MII	MI_v_mitoM	MI_v_pro	MII_v_MI	MII_v_mitoM	MII_v_pro	mitoM_v_MI	mitoM_v_MII	mitoM_v_pro
SPC42_326	SPO74_154	MRH1_295	PES4_58	MRH1_295	ISW1_1061	SPC42_326	MRH1_295	NET1_676	SPC42_326	KIP2_26	NET1_676
SSZ1_477	RFA1_178	RSC2_682	SPO74_154	MRH1_289	NET1_676	NUD1_468	MRH1_289	SEC4_201	SSZ1_477	HRK1_37	VTC2_182
SPT6_155	CTR1_317	MRH1_289	CTR1_317	NMA1_13	GAL4_724	IST2_704	NMA1_13	NDC1_412	CUE5_364	ASK10_1070	VID27_207
BRN1_254	RAD52_302	CBF5_378	REG1_254	RGA1_749	NDC1_412	YDL186W_102	CBF5_378	IKS1_299	GPH1_31	DGR2_716	CNM67_89
SPC42_213	GCD2_21	HIR2_460	BUD6_342	CBF5_378	BBP1_84	TSL1_155	RSA3_2	SEC4_204	YDR186C_692	EIS1_130	NET1_1032
IOC4_242	RPN1_24	NMA1_13	TRI1_79	HIR2_460	SWI6_149	ERB1_23	NMD3_427	HPR1_694	KIP2_26	SRC1_233	NDC1_412
SDS3_230	SEC21_638	MCD1_354	KRI1_35	GSY1_651	ADY3_38	SEC4_204	RSC2_682	GYL1_37	VTC2_583	REG1_75	VTC2_187
PRP43_38	BBP1_42	GSY1_651	CDC5_70	GSY2_651	ISW1_1082	ADY3_72	HIR2_460	SWH1_755	DGR2_716	RPN1_24	ISW1_1061
BIM1_139	MRK1_326	GSY2_651	CDC5_73	GSY1_655	SKO1_559	MPP10_177	GSY1_651	ADY3_38	IPP1_266	NAB6_464	DIG2_225
ARP8_237	CMD1_82	SWH1_693	RIF1_1755	GSY2_655	SWH1_755	SEC4_201	GSY2_651	BBP1_84	NUD1_468	XRS2_349	NUP60_171
RAD52_302	INP53_1061	GSY2_655	RGA1_735	RSC2_682	HPR1_694	DON1_166	GSY1_655	HBT1_669	SPN1_89	DIG2_225	GPH1_31
ATO2_22	KIN2_22	LEO1_358	SEC21_638	RSA3_2	HBT1_669	SSZ1_477	TRI1_113	RPL24B_86	REG1_75	NUP60_171	YDR186C_692
REC8_421	HOS4_688	GSY1_655	ADY3_234	EDE1_931	UME6_350	ARP8_65	RPG1_220	STM1_41	SET3_684	DNM1_629	BBP1_84
YSC84_301	FIP1_50	EDE1_931	SPC29_58	ABP1_181	SEC7_1736	BFR1_336	RGA1_749	SEC7_1736	HRK1_37	CUE5_364	BRE2_160
GCD2_21	ATO2_22	TRI1_113	PFK1_189	TRI1_113	ADY3_117	ASK10_344	NAP1_82	TYS1_359	EIS1_130	RQC1_119	DGR2_716
RPN1_19	STV1_223	PCT1_346	NAB6_464	TRA1_542	HFM1_100	ADY3_256	TPS3_181	CNM67_89	XRN1_1510	SPC42_32	XRN1_1510
RFA1_178	SWI3_88	SPC42_213	XRS2_349	TDA11_247	BRE2_160	DON1_224	GSY2_655	RPG1_893	POM34_273	IVY1_59	MIH1_82
SDA1_278	SPT6_155	RSA3_2	SPO21_119	YTA7_1300	NAP1_82	MID2_260	SEC7_1736	NAP1_82	ACE2_80	CNM67_120	BBP1_81
SSZ1_480	PUP2_56	RGA1_749	SPC29_183	PWP2_664	NET1_1032	YPR174C_77	TDA11_247	SNF1_487	SSZ1_480	SPC42_357	DCP2_751
SMC4_31	DTR1_315	ABP1_181	FBP1_12	NMD3_427	DIG2_266	RIM4_339	CBF5_416	NET1_1032	ASK10_1070	PDA1_313	GPD1_24

Figure 8-figure supplement 1. Identification of phospho-sites co-isolated with purified kinetochores in meiotic prophase, metaphase I, metaphase II and mitotic metaphase. (A) Barplot of the number of phospho-sites quantified in each Dsn1-6His-3Flag immunoprecipitation. (B) Venn diagram of the number of phospho-sites identified in each Dsn1-6His-3Flag immunoprecipitation and whether they were unique to sample type or

1524 shared between groups. A phospho-site was included in a group if it was detected in all
1525 replicates of that sample type. (C) GO term enrichment of the selected terms among the top
1526 50 non-kinetochore phospho-proteins co-purified at each stage. (D) Top 20 non-kinetochore
1527 phospho-sites, ranked by increasing fold change enrichment in the first stage listed vs the
1528 second stage. (For example prophase vs MI, phospho-sites are ranked by enrichment in
1529 prophase.)
1530

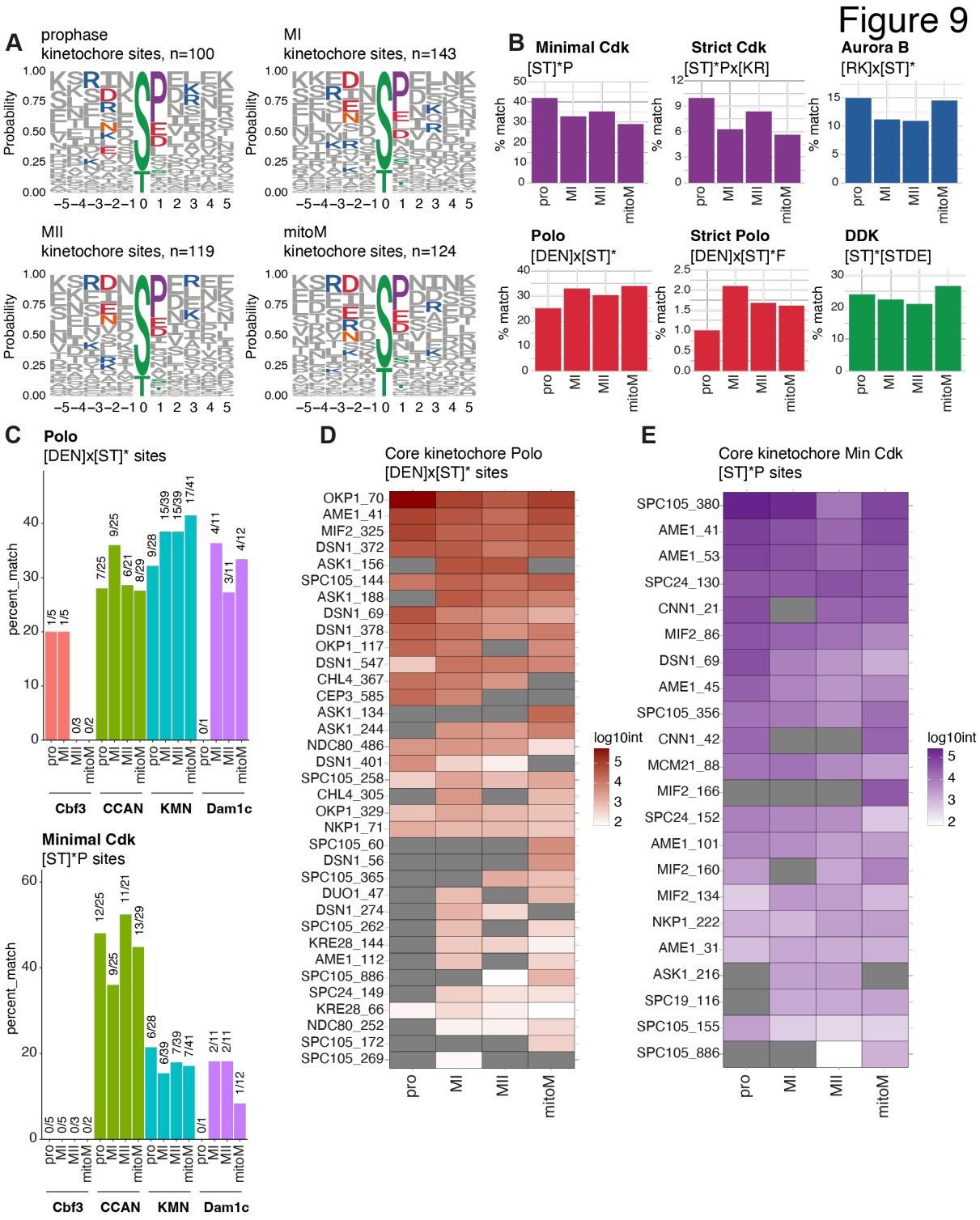

Figure 9 Kinetochore phospho-site motifs do not vary significantly by stage

(A-D) Features of kinetochore phosphorylation after phospho-analysis of kinetochore purifications in Figure 5. (A) Motif logos of amino acids surrounding kinetochore protein phospho-sites at each stage. (B) Barplots of the percent of phospho-sites which match indicated kinase consensus motifs at each stage. (C) Barplots of the percent of phospho-sites which match the Polo kinase consensus motif (top) or minimal Cdk consensus motif (bottom),

1538 sorted by kinetochore sub-complex and cell cycle stage. (D) Heatmap showing the abundance
1539 of individual kinetochore phospho-sites matching the minimal Polo kinase consensus. (E)
1540 Heatmap showing the abundance of individual kinetochore phospho-sites matching the
1541 minimal Cdk kinase consensus.